



**National Institute of Standards and Technology**  
Technology Administration, U.S. Department of Commerce

***NIST Technical Note 1528***

**The Impact of Internal Sampling  
Circuitry on the Phase Error  
of the Nose-to-Nose  
Oscilloscope Calibration**

**Kate A. Remley**



# ***NIST Technical Note 1528***

## **The Impact of Internal Sampling Circuitry on the Phase Error of the Nose-to-Nose Oscilloscope Calibration**

Kate A. Remley

*Radio-Frequency Technology Division  
Physics Laboratory  
National Institute of Standards and Technology  
325 Broadway  
Boulder, Colorado 80305*

August 2003



**U.S. Department of Commerce**

*Donald L. Evans, Secretary*

**Technology Administration**

*Phillip J. Bond, Under Secretary of Commerce for Technology*

**National Institute of Standards and Technology**

*Arden L. Bement, Jr., Director*

Certain commercial entities, equipment, or materials may be identified in this document in order to describe an experimental procedure or concept adequately. Such identification is not intended to imply recommendation or endorsement by the National Institute of Standards and Technology, nor is it intended to imply that the entities, materials, or equipment are necessarily the best available for the purpose.

National Institute of Standards and Technology Technical Note 1528  
Natl. Inst. Stand. Technol. Tech. Note 1528, 68 pages (August 2003)  
CODEN: NTNOEF

U.S. GOVERNMENT PRINTING OFFICE  
WASHINGTON: 2003

---

For sale by the Superintendent of Documents, U.S. Government Printing Office  
Internet: [bookstore.gpo.gov](http://bookstore.gpo.gov) Phone: (202) 512-1800 Fax: (202) 512-2250  
Mail: Stop SSOP, Washington, DC 20402-0001

## Contents

1. Introduction .....	1
1.1 Background .....	2
1.2 Overview of the Parametric Study .....	4
2. Theory of the Nose-to-Nose Calibration .....	4
2.1 Sampler Theory .....	5
2.2 Nonideal Sampling and the “Impulse Response” .....	6
2.3 The Kickout Pulse .....	8
2.4 Nose-to-Nose Calibration .....	9
3. Large- and Small-Signal Analysis of the Sampling Circuit .....	12
3.1 Diode Models .....	12
3.1.1 Large-Signal Model .....	12
3.1.2 Small-Signal Model .....	14
3.2 Diode-Related Errors in the Nose-to-Nose Calibration .....	16
3.2.1 Diode Conductance .....	18
3.2.2 Nonlinear Diode Junction Capacitance .....	18
4. SPICE Simulations .....	19
4.1 SPICE Models .....	20
4.1.1 Riad’s Model .....	21
4.1.2 Kerley’s Model .....	21
4.2 Development of the Default Sampling-Circuit Model .....	22
4.2.1 Packaging Parasitics .....	25
4.2.2 Strobe-Excitation-Pulse Rise Time .....	26
4.3 SPICE Convergence Studies .....	27
4.3.1 Time Step .....	29
4.3.2 Sampling-Cycle Period .....	30
4.3.3 Input Voltage Level .....	31
4.3.4 Input Pulse Width .....	31
4.4. More Details on the SPICE Simulations .....	32
4.4.1 Impulse Response Calculations .....	32
4.4.2 Kickout Pulse Calculations .....	33
4.4.3 Nose-to-Nose Calculation and Error .....	33
Appendix for Section 4. SPICE Code .....	35
5. Parametric Studies Using SPICE .....	39
5.1 Sampling Diode Model Parameters .....	39
5.1.1 Description .....	39
5.1.2 Simulation Results .....	40
5.1.2.1 Diode Model Parameters Except Junction Capacitance .....	40
5.1.2.2 Parameters Including Diode Junction Capacitance .....	41
5.1.2.3 Split Diode Model .....	42
5.2 Hold Capacitors .....	43
5.2.1 Description .....	43
5.2.2 Simulation Results .....	44
5.3 Strobe-Generator Impedance and Strobe Pulse-Shaping Circuitry .....	44
5.3.1 Ideal Source and Transmission Line Pulse Shaping .....	44

5.3.1.1 Description.....	44
5.3.1.2 Simulation Results .....	46
5.3.2 Strobe-Pulse Rise Time.....	46
5.3.2.1 Description.....	46
5.3.2.2 Simulation Results .....	46
5.3.3 Strobe-Generator Impedance.....	47
5.3.3.1 Description.....	47
5.3.3.2 Simulation Results .....	48
5.3.4 Strobe-Excitation-Pulse Amplitude .....	49
5.3.4.1 Description.....	49
5.3.4.2 Simulation Results .....	49
5.4 Diode Imbalance .....	50
5.4.1 Description .....	50
5.4.2 Simulation Results .....	51
5.5 Diode Bias Level.....	52
5.5.1 Description .....	52
5.5.2 Simulation Results .....	53
5.6 Input Network Impedance .....	54
5.6.1 Description .....	54
5.6.2 Simulation Results .....	54
Appendix for Section 5. Error Pulses.....	56
6. Sensitivity Analysis and Standard Uncertainty .....	57
6.1 Ranking the Contributions to the Phase Error.....	57
6.2 Estimate of Standard Uncertainty Due to Combined Sampling Circuitry Variation .....	60
6.3 Summary and Conclusions.....	62
References .....	63



# **The Impact of Internal Sampling Circuitry on the Phase Error of the Nose-to-Nose Oscilloscope Calibration**

Kate A. Remley

National Institute of Standards and Technology  
Radio-Frequency Technology Division  
325 Broadway  
Boulder, CO 80305

We discuss the dependence of the phase error in the nose-to-nose oscilloscope calibration on the oscilloscope's sampling circuitry. We first present the theory behind the nose-to-nose calibration, and then present both large- and small-signal analyses of the sampling circuit. Using this background information, we develop a sampling-circuit model. We then carry out parametric studies in which we systematically vary the component values of the internal sampling circuit. From these studies, we determine which components of the sampling circuitry of the oscilloscope contribute most significantly to errors in the nose-to-nose calibration. We then predict an expected range of phase errors from a range of realistic component values.

**Keywords:** Electrical Phase; Large-Signal Network Analyzer Calibration; Nose-to-Nose Calibration; Oscilloscope Calibration; Phase Calibration; Sampling Circuit; Schottky Diode; SPICE Model.

## **1. Introduction**

The nose-to-nose calibration technique [1-4] was proposed in 1990 to determine the impulse response of broadband oscilloscopes. Finding and correcting the response of these high-speed oscilloscopes is important because the typical response time of their internal sampling circuitry is of the same order as the signal transitions of many high-speed circuits under test. To measure the amplitude response of broadband (defined here as 20 GHz or greater) sampling oscilloscopes, we currently use the "swept-sine" method [2, 5], where a series of individual tones of increasing frequency and known power are fed into the oscilloscope. The power in the tones is measured with a power meter traceable to NIST. Comparing the known amplitude of the input signal to the signal measured by the oscilloscope allows us to determine and correct the magnitude response of the oscilloscope.

However, the phase response of an oscilloscope, that is, the unintentional change in the phase relationships between frequency components of a signal caused by the oscilloscope itself, has presented a more difficult challenge. The nose-to-nose calibration currently represents one practical method for estimating an oscilloscope's phase response.

In this report, we perform a parametric sensitivity study of the internal sampling circuitry found in the type of broadband oscilloscope that is used in nose-to-nose calibrations. This numerical study has three primary objectives: (1) developing a method to predict the nose-to-nose phase response arising from the internal sampling circuitry of the oscilloscope that is robust and can be easily extended; (2) ascertaining which components of the internal sampling circuitry of the oscilloscope contribute most significantly to errors in the estimated phase response provided by the nose-to-nose calibration; (3) predicting an expected range of phase errors from a range of realistic component values. This third point is important because we have no way of knowing the exact component and parameter values for the sampling circuit due to measurement limitations, fabrication tolerances, and manufacturer proprietary issues. However, we can estimate a realistic *range* for component values based on the literature. Simulating the nose-to-nose calibration over this range gives us an estimate of the expected range of the errors in the phase response due to the sampling circuitry. The methodology we develop can easily be applied to other sampling-circuit representations.

This study is based on numerical simulations of a representative sampling-circuit model. It yields information we would have difficulty obtaining through other methods. For example, unambiguous measurements of the response of the internal circuitry of high-speed samplers is extremely difficult to carry out. As well, simulations enable parametric variation of circuitry that would be impossible to conduct experimentally due to limitations in component fabrication and measurement technology. Thus, parametric variation within numerical simulations offers insight into sampling-circuit-related error mechanisms in the nose-to-nose calibration that otherwise would not be available.

## 1.1 Background

Over a decade ago, researchers at a manufacturer of digital oscilloscopes noticed that when a DC offset was applied to bias lines of their oscilloscope by changing the “DC offset” setting, a short “kickout” pulse appeared at the input port. This pulse is almost identical in shape to the time-domain “impulse” response of the oscilloscope itself. When the input ports of two identical oscilloscopes of this type are connected “nose-to-nose,” the similarity of the kickout pulse and impulse response can be used to extract the response of one of the oscilloscopes. In practice, since no two oscilloscopes are truly identical, a series of three measurements is made on three oscilloscopes to extract the response. Knowledge of the response can subsequently be used to correct waveforms measured with the oscilloscope.

One important use for the nose-to-nose calibration is for phase calibration of certain types of nonlinear vector network analyzers (LSNAs). LSNAs allow measurement of the phase and amplitude response of nonlinear circuits and systems subjected to periodic stimuli. The nose-to-nose calibration enables correction of the phase of measured harmonic components relative to the fundamental. A transfer standard (typically a “reference” or “comb” generator that is rich in harmonic content) is first measured using a nose-to-nose-calibrated oscilloscope. The comb generator is then connected to the LSNA and the phase relationships of the comb generator harmonics are



measured on the LSNA. Since the phase relationships of the comb generator are known from the nose-to-nose-calibrated oscilloscope measurement, correction factors for the LSNA can be extracted and subsequent LSNA measurements corrected. Correction of the phase relationship between the fundamental and harmonics of DUTs measured on LSNA's up to 50 GHz is currently accomplished using this method, although most LSNA's are currently limited to an upper frequency of 20 GHz.

Other methods for correcting the phase response of broadband sampling oscilloscopes include measuring a well-characterized waveform with the oscilloscope. The output of the oscilloscope is a convolution of this known signal and the impulse response of the oscilloscope. Once the impulse response of the oscilloscope is deconvolved from the measured signal, correction coefficients are extracted from the difference between the known and measured signals [6, 7]. Both NIST and NPL (National Physical Laboratory, in the United Kingdom) have measurement services based on this approach.

Electro-optic sampling (EOS) systems [8] offer a method of characterizing pulses with very large bandwidths [9, 10]. Because these systems are based on on-wafer methods and fast optoelectronic interactions, they have measurement bandwidths in the terahertz range. These known pulses can then be used to calibrate an oscilloscope to even higher frequencies than the methods currently in use discussed above.

An experimental method for correcting the phase response of an oscilloscope or an LSNA involves measuring a reference nonlinear circuit such as a "golden diode" [11] with the oscilloscope or LSNA we wish to calibrate. If the phase relationship between the fundamental and the harmonics appearing at the output of the reference circuit is known, we can measure the reference circuit and correct the measurement. The problem with this technique is that, to date, no phase standard with sufficient bandwidth, stability, and known phase response has been developed for broadband oscilloscopes. This is a topic of current research at NIST and a few other labs.

The nose-to-nose calibration is a variation of the first method described above. In this case, the "known" pulse is the kickout pulse, which is assumed to have essentially the same shape as the impulse response of the oscilloscope itself. The method has the advantage of requiring very little custom equipment and its sources of uncertainty have been studied in depth. Several researchers have investigated experimental sources of error in the nose-to-nose calibration [2-5, 12, 13]. Others have provided analytic analyses of errors introduced by the sampler circuitry of the oscilloscope itself [14, 15]. In this report, we turn to SPICE-based numerical simulation of a realistic model of the sampling circuit [16, 17] (SPICE is an acronym for "Simulation Program with Integrated Circuit Emphasis." The SPICE3 program that we use was developed by researchers at the University of California at Berkeley.) Simulation allows us to better identify error mechanisms involving the internal sampling circuitry and to understand the sensitivity of the oscilloscope's phase response to parametric changes in sampling-circuit component values. We develop procedures to quantify the sensitivity of the phase error to each

component and to a combination of components, and then apply these procedures to our simulation results.

## 1.2 Overview of the Parametric Study

In Sections 2 and 3, we discuss the theory of the nose-to-nose calibration and provide large- and small-signal models of the internal sampling circuitry found in the type of oscilloscope used in nose-to-nose calibrations. In Section 4, we discuss our implementation of a SPICE model of the sampling circuitry. We calculate a nominal value for the “phase error” associated with this default sampler configuration, where we define the phase error as the difference in the phase of the sampling circuit’s impulse response, derived by the nose-to-nose procedure, from its actual value. For the default sampling-circuit configuration that we examined, our phase error is approximately  $3.3^\circ$  at 20 GHz. In Section 5, we then vary the parameters of the model one at a time, note the effect (increase or decrease) on the phase error, and discuss the reasons for the change in phase error. From this systematic parametric variation, we determine which circuit components contribute most significantly to the phase error in the nose-to-nose calibration, and rank these contributions in Section 6.

Finally, even though we don’t know the exact values of sampling-circuit components we can find the range of predicted phase errors, given a sampling-circuit model and an expected realistic range of component values. To do this, we systematically vary all circuit component values over a given range (for example,  $\pm 10\%$  of the value specified in our default sampling-circuit model) and find the corresponding maximum and minimum phase error. Assuming that the distribution of phase errors over this range is uniform, we calculate the standard deviation and the standard uncertainty. For our sampling circuit, the value of our standard uncertainty is approximately  $1.4^\circ$  (that is, for our particular set of sampling-circuit parameters, our phase error is approximately  $3.3^\circ$  and the standard uncertainty of the predicted phase error is  $\pm 1.4^\circ$ ). This procedure can easily be extended to models where component values are known in greater detail, leading to a better approximation of the phase error in the nose-to-nose calibration due to internal sampling-circuit effects.

In this work, we have attempted to provide as accurate a model of the oscilloscope’s sampling circuit as possible, although the model is strictly an approximation. Thus, while we do provide an *estimate* of the phase error, we make no exact statement of the phase-error value arising from the sampling circuitry in a real oscilloscope. However, as mentioned above, our procedure could easily provide a better estimate of the phase error if the model and component values were known in greater detail. We are also able to provide important information on phase-error mechanisms arising from the internal sampling circuitry that cannot be obtained elsewhere.

## 2. Theory of the Nose-to-Nose Calibration

In this section, we discuss the fundamental premise of the nose-to-nose calibration: that the “impulse response” of a sampler is equivalent to the “kickout pulse”

that is generated by the sampler when a DC offset is applied. We describe how an estimate of the impulse response of the sampler is derived from the nose-to-nose response, and we define a representation of the error in the calibration that tells us how different the actual impulse response is from the estimate.

To understand the theory of the nose-to-nose calibration, it is useful to understand the operation of the internal sampling circuits used in the applicable type of broadband oscilloscope. This description is given in Section 2.1 below, where we describe basic sampling operation and differentiate between large-signal and small-signal regimes in the sampler. We define the sampler's impulse response in Section 2.2, and the kickout pulse in Section 2.3. In Section 2.4, we describe the nose-to-nose technique and define the error in a nose-to-nose estimate. We limit our discussion to the role of the samplers in the nose-to-nose calibration, since other possible sources of phase error, such as mismatch corrections and time-base distortion, are treated elsewhere [2, 3, 5, 12, 13].

## 2.1 Sampler Theory

Figure 2-1 depicts a simplified schematic diagram of a two-diode balanced sampling circuit. This type of two-diode sampling circuit is required for performing a nose-to-nose calibration, since it generates a kickout pulse that is related to its impulse response. The bias supplies,  $V_b$ , place the diodes in a high-impedance reverse-biased state until the strobe fires. Each time the strobe fires, the strobe pulse forward biases the two diodes, turning them on and lowering their impedances for a short time. Because the large-signal strobe current flows in one direction only (shown by solid arrows in Fig. 2-1) and the circuit is balanced, the effects of the strobe current cancel at the input port of the sampling circuit, that is,  $I_{\text{strobe}} + I_{\text{inverted strobe}} = 0$  at the input node.

While the diodes are in their low-impedance state, a nonzero voltage at the input port of the sampling circuit causes a net charge to flow from the input port through the diodes to the hold capacitors. This small-signal current (shown by dashed arrows in Fig. 2-1) flows in opposite directions in the two diodes, and adds a net charge on the hold

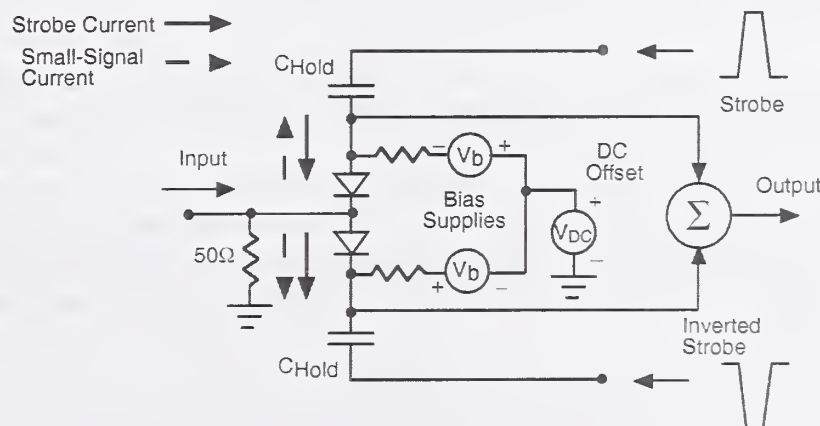


Figure 2-1. Simplified schematic of a two-diode sampling circuit.



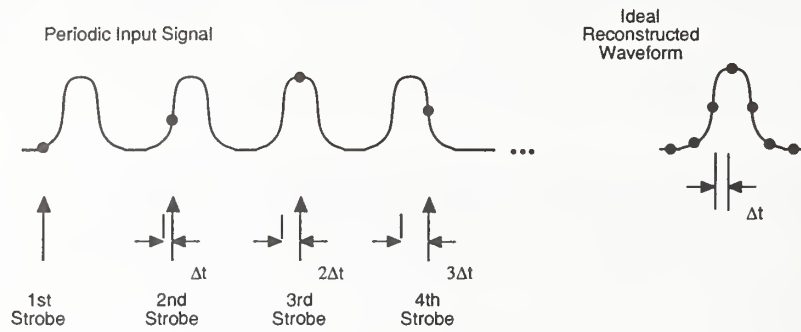


Figure 2-2. Ideal sequential sampling and reconstruction of the discretized input signal.

capacitors. The sampler discretizes the average voltage on the two hold capacitors after the strobe fires. This discretized voltage sample is proportional to the net charge transferred to the hold capacitor when the strobe fired, and ideally will be proportional to the voltage at the input port when the strobe fired.

In sequential sampling [18], a periodic input signal—that is, a repetitive train of identical waveforms—is applied to the input port. The sampling circuit is used to reconstruct the shape of a portion of the periodic input signal. This is accomplished by firing the strobe at a time  $\Delta t$  later than it was fired in the previous cycle of the periodic input signal, as shown in Fig. 2-2. (Equivalently, the strobe may fire at a time  $nT \pm \Delta t$  different from its previous firing, where  $n$  is an integer and  $T$  is the period [repetition rate] of the input signal. For clarity in this description, we describe this process in terms of  $t_0 + n\Delta t$ ,  $t_0$  = initial strobe,  $n = 1, 2, \dots$ ). In this way the strobe's firing time slowly "scans" across the input waveform being sampled. Since each successive discretized voltage sample corresponds to the input voltage at a time  $\Delta t$  later than the previous voltage sample, the shape of the individual waveforms in the periodic input signal can be reconstructed from the discretized output voltage record.

## 2.2 Nonideal Sampling and the "Impulse Response"

If the diodes injected charge onto the hold capacitors only at the instant that the strobe fired, the shape of the reconstructed signal at the output of the sampling circuit would exactly mirror the shape of the individual waveforms in the periodic input signal. However the strobe pulses have a finite duration and the diodes do not turn on or off instantaneously. Hence, charge is injected on the hold capacitors in a nonuniform way over a finite period that may be significantly longer than the sampling interval  $\Delta t$ . As a result, the nonideal response of the sampling circuit alters the reconstructed output, as shown in Fig. 2-3.

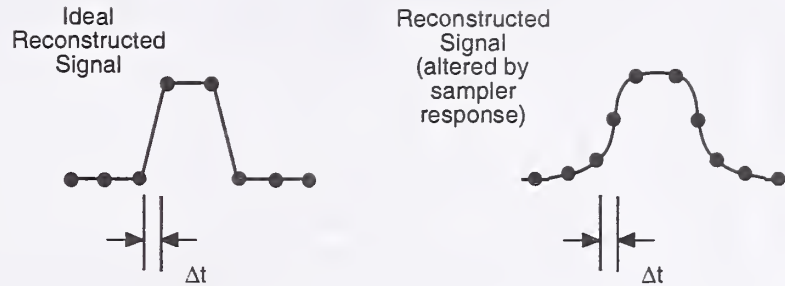


Figure 2-3. Ideal sampling compared to sampling altered by the sampler's response.

In general, practical samplers are neither linear nor time invariant. However, the process of charge injection is nearly linear for small input signals. As a result, we find that the reconstructed signal can be described as a convolution of an individual pulse at the input port with a function we will call the “impulse response” of the sampling circuit. While this function is clearly not an impulse response in the strict sense, we will call it that because we expect its properties to be similar to those of the impulse response of a truly linear time-invariant circuit. That is, we expect the output of the sampling circuit to be equal to the convolution of the input signal and its impulse response. Equivalently, the output of the sampling circuit can be represented as the product of a frequency-domain transfer function and the frequency-domain representation of the input signal. It is the impulse response or, equivalently, frequency-domain transfer function that we wish to determine and correct using the nose-to-nose technique.

To test the hypothesis that the output response of the sampling circuit is a convolution, we inserted the circuit values for the sampler described in Ref. [19] into a SPICE model of the sampling circuit shown in Fig. 2-1 [16]. This model includes a full nonlinear diode model and diode-package parasitics. To determine the impulse response of the sampling circuit, we applied a train of very narrow pulses (0.5 ps rise time, fall time, and pulse width) to its input. The spectrum corresponding to these pulses is very broad with roll-off frequencies much higher than the 20 GHz input bandwidth of our sampler. Then we numerically deconvolved this narrow pulse from the circuit's response to the input pulse train, as shown in the curve labeled “Impulse Response” in Fig. 2-4.

To verify that the reconstructed output of our sampling circuit is indeed the convolution of this impulse response and an arbitrary input signal, we compared numerical convolutions of the impulse response and a single pulse in the input pulse train to the output responses of the circuit when excited by this input signal. Figure 2-4 shows some typical results. In all the cases we tested, we found that the output responses were nearly identical to the convolutions. This lends credence to the somewhat unusual notion of impulse response employed in Refs. [2-4] that we use here.



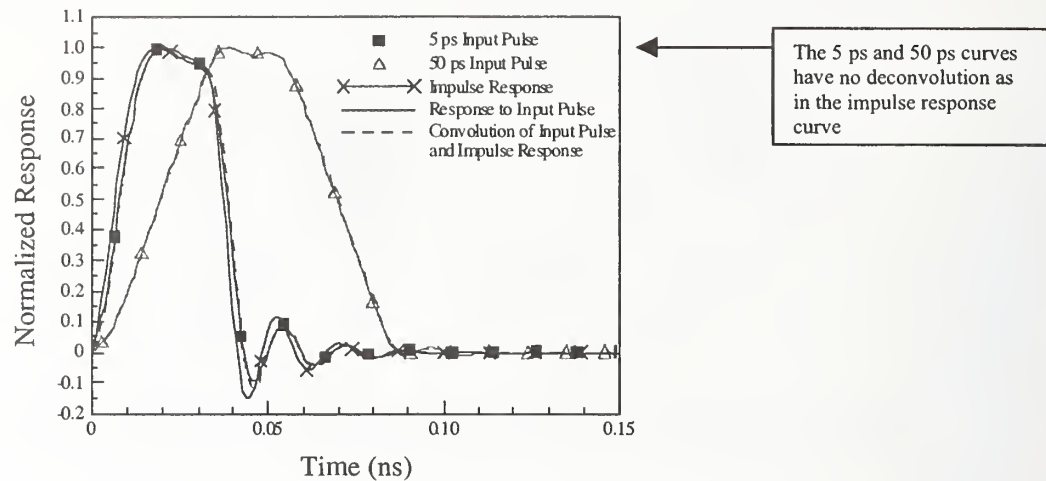


Figure 2-4. Impulse response of a sampling circuit (solid line with crosses) determined by deconvolving narrow input pulses from the output of the sampling circuit simulation. The figure also compares the output response of the sampling circuit (solid lines) when excited with input pulses of 5 ps and 50 ps duration to convolutions (dashed lines) of the input pulse and the impulse response. The 5 ps and 50 ps pulses are not deconvolved, as the input pulse is for the Impulse Response curve.

## 2.3 The Kickout Pulse

Rush, Draving, and Kerley [1] noted that when the DC offset voltage (see Fig. 2-1) for a sampling circuit of this design is nonzero, it creates a train of “kickout” pulses at its input port with a shape similar to that of the circuit’s impulse response. Figure 2-5 compares a kickout pulse created by our SPICE circuit (solid black line with inverted triangles) to its impulse response (solid green line). The figure shows that the two signals are indeed similar.

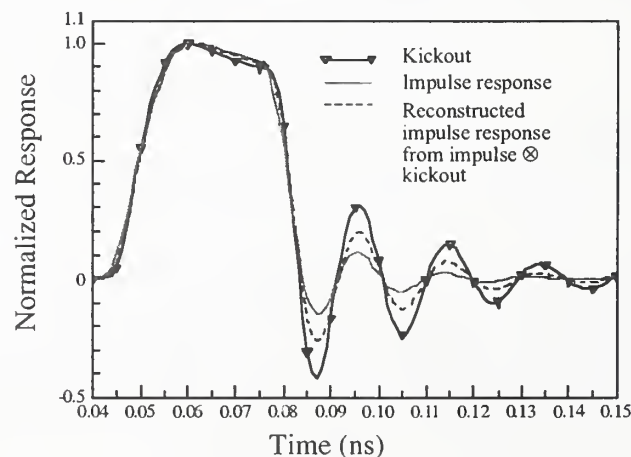


Figure 2-5. Typical results when we compare the kickout pulse, the impulse response, and an estimate of the impulse response reconstructed from a convolution of the impulse response and the kickout pulse. This reconstruction is the basis of the nose-to-nose calibration.

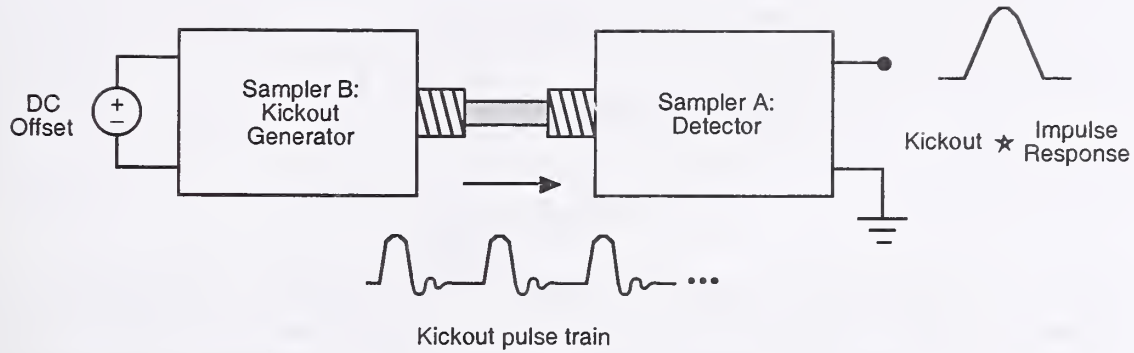


Figure 2-6. The configuration used to implement the simplified nose-to-nose calibration procedure for identical sampling circuits connected by a reflectionless through connection. The output of Sampler A is called the nose-to-nose response. This response should be equal to the convolution of the kickout pulse of Sampler B and the impulse response of Sampler A for small-signal inputs.

## 2.4 Nose-to-Nose Calibration

The nose-to-nose calibration [1-4] exploits the similarity of the kickout pulses and the impulse response. Figure 2-6 illustrates a simplified nose-to-nose procedure. The idea is to set the DC offset voltage of one sampling circuit, which we will call B, to a nonzero value so that it creates a train of kickout pulses at its input port. These pulses are fed into the input port of a second sampling circuit, which we will call A, operating in its conventional sampling mode. We will call the output of A the nose-to-nose response of the two sampling circuits.

As discussed above and as shown in Refs. [2-4, 16] and [17], in the absence of reflections or mismatches, the response of the entire system is proportional to the convolution of the time-domain representation of the impulse response of Sampler A and the kickout of Sampler B. In the frequency domain we have

$$M(\omega)_{AB} \propto K_B(\omega)H_A(\omega), \quad (2-1)$$

where  $M_{AB}$  is the Fourier transform of the measured waveform,  $H_A$  is the Fourier transform of the impulse response of Sampler A and  $K_B$  is the Fourier transform of the kickout pulse emanating from Sampler B. We define the Fourier Transform as  $F(\omega) = \int_{-\infty}^{\infty} f(t)e^{-j\omega t} dt$ , with  $\omega = 2\pi f$  and  $f$  the frequency in Hertz. In our numerical simulations we use the Fast Fourier transform (FFT), a time- and frequency-discretized version of the Fourier transform.

For identical, impedance-matched samplers, such as those we used in the simulations described in this report,  $K_A(\omega) = K_B(\omega)$ ,  $H_A(\omega) = H_B(\omega)$ . In this case,

$$\begin{aligned}
H_A(\omega)^{\text{est}} &\equiv C\sqrt{K_B(\omega)H_A(\omega)} \\
&= CH_A(\omega)\sqrt{\frac{K_B(\omega)}{H_A(\omega)}} \\
&= CH_A(\omega)\sqrt{\frac{K_B(\omega)}{H_B(\omega)}},
\end{aligned} \tag{2-2}$$

where  $C$  is a simple proportionality constant required because the amplitudes of the kickout and impulse response are not identical. However, in practice, no two sampling circuits are identical. In this case, an estimate of the impulse response of Sampler A can be found from a set of three measurements of three samplers [3]

$$\begin{aligned}
H_A(\omega)^{\text{est}} &\equiv C\sqrt{\frac{M_{AB}(\omega)M_{AC}(\omega)}{M_{BC}(\omega)}} \\
&\equiv CH_A(\omega)\sqrt{\frac{K_B(\omega)}{H_B(\omega)}}.
\end{aligned} \tag{2-3}$$

Note that other combinations of samplers also will produce the estimate for sampler A.

In both eqs (2-2) and (2-3), the term  $C\sqrt{K_B(\omega)/H_B(\omega)}$  expresses the deviation of the estimate from the actual impulse response. We define an (inverse) correction factor  $E(\omega)$  of the Fourier transform of the impulse response estimate as

$$E_A(\omega) \equiv \frac{H_A^{\text{est}}(\omega)}{H_A(\omega)} \equiv C\sqrt{\frac{K_B(\omega)}{H_B(\omega)}}, \tag{2-4}$$

where we chose  $C$  such that  $E(0) = 1$ , with  $\omega = 0$ , the DC point. To accurately represent the impulse response of an oscilloscope, the impulse response estimate generated by a series of nose-to-nose measurements should be divided by the correction factor  $E(\omega)$ . This correction factor (assuming linearity; reciprocal, reflectionless connection networks; and a perfect oscilloscope timebase) can be approximated as the square root of the Fourier transform of the kickout pulse divided by the sampler's impulse response. Note that  $E(\omega)$  is related to the relative or fractional error since

$$\text{Relative Error} = \frac{H_A - H_A^{\text{est}}}{H_A} = 1 - \frac{H_A^{\text{est}}}{H_A}. \tag{2-5}$$

If the kickout pulse and impulse response were identical, the correction factor in eq (2-4) would equal one, and we would expect the nose-to-nose reconstruction to be equal to the impulse response. However, Fig. 2-5 shows that the kickout pulse and impulse response of our sampling circuit are not identical. The figure compares these to the reconstruction of the impulse response from the convolution of the kickout pulse and impulse response, and shows that the reconstruction is, in fact, an average of the sampling circuit's kickout pulse and its impulse response, as predicted by Ref. [2] and defined by the convolution procedure. Since the kickout pulse and impulse response are

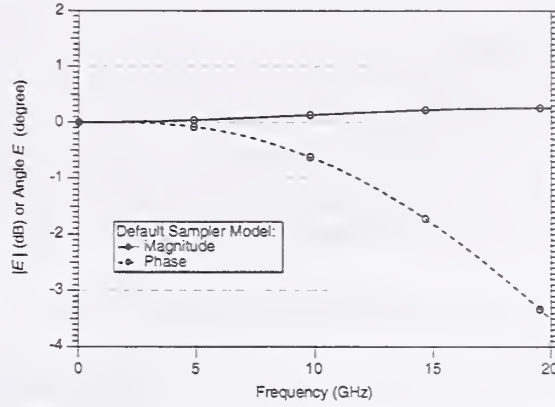


Figure 2-7. Magnitude and phase component of the correction factor  $E(f)$  for one model of the sampling circuit. The curves represent the difference between the impulse response of the sampler and the nose-to-nose derived estimate of the impulse response, defined in eqs (2-6) and (2-7).

not identical (and, in the real world we can't know each of these independently), the reconstructed impulse response is somewhat in error. Throughout this work, we use the correction factor to specify the magnitude error in the nose-to-nose calibration as

$$|E_A(f)| = C \sqrt{\frac{K_A}{H_B}} \quad (2-6)$$

in decibels, and the phase error as

$$\arg\{E_A(f)\} = [\arg\{K_B(f)\} - \arg\{H_B(f)\}] / 2 \quad (2-7)$$

in degrees, with  $f = \omega/2\pi$ . Again, subscripts A and B refer to two different samplers. As stated above, we use identical samplers in our modeling work and thus  $K_A(f) = K_B(f)$ ,  $H_A(f) = H_B(f)$ , and  $E_A(f) = E_B(f)$ .

In the simulations that follow, calculations were performed in the time domain in SPICE and then transformed to the frequency domain using the fast-Fourier transform (FFT) procedure. The sampler's impulse response was derived using the method of Section 2.2 and compared to the FFT of a nose-to-nose derived impulse response (Section 2.3), which generates the correction factor  $E(f)$ , defined in eq (2-4). The magnitude and phase components were calculated as in eqs (2-6) and (2-7), the phase component was detrended (see below) and the two were plotted in graphs, such as the one shown in Fig. 2-7 for the SPICE model of the sampler described in Section 4.2.

Throughout the remainder of this work we will focus on the phase error defined in eq (2-7), an example of which is shown by the dashed line in Fig. 2-7. Because the sampler introduces an arbitrary time shift into a signal that passes through it (simulated or measured), we first subtract this time shift from our error ratio vector data, without loss of generality. A simple time shift (delay),  $t_0$ , is equivalent to multiplication by  $e^{-j2\pi f t_0}$  in the frequency domain, which introduces a linear slope  $2\pi f t_0$  into the phase error  $\arg\{E(f)\}$ .



To determine the value of  $2\pi t_0$ , we numerically differentiated the phase-error vector with respect to frequency. We chose  $2\pi t_0$  to correspond to the value of the differentiated phase-error vector at DC, and subtracted it from the phase error to set its slope to zero at DC. We then integrated to transform back to the frequency domain. Note that while this alignment procedure is straightforward for simulated data, it is typically much more difficult for noisy, measured data since numerical differentiation can significantly increase the noise content in the phase-error vector.

### 3. Large- and Small-Signal Analysis of the Sampling Circuit

The diodes in a sampling circuit function as voltage-controlled switches, enabling charge to flow to the hold capacitors only for the brief instant that the strobe pulse amplitude exceeds the diode's threshold voltage. In theory, if the diodes behaved as perfect switches, the nose-to-nose calibration would be exact [3, 15, 20]. However, all diodes have an inherent voltage-dependent nonlinear junction capacitance and a conductance that is an asymmetric function of time. These effects and their interaction with impedances in the circuit cause the kickout pulse to be somewhat different in shape from the impulse response, with the nonlinear junction capacitance having greater impact [15, 20]. As a result, the nose-to-nose calibration in its present form will contain errors.

We devote this section to a description of the diodes and a discussion of the potential error mechanisms due to the effects discussed above. We describe the way sampling diodes are modeled in SPICE and how we extract additional important quantities, such as the diode conductance, from the SPICE simulations. We examine the reason why the asymmetric diode conductance is not a significant source of error, and why the nonlinear diode junction capacitance does introduce errors into the nose-to-nose calibration. This discussion sets the background for the parametric study presented in Section 5.

#### 3.1 Diode Models

The Schottky-barrier diode models used in our simulations are shown in Fig. 3-1. These common models are found in, for example, Ref. [21]. Because both the large- and small-signal regimes are important to our discussion of sampling circuits and the nose-to-nose calibration, we discuss each separately.

##### 3.1.1 Large-Signal Model

The large-signal representation in Fig. 3-1(a) models the diode junction as a voltage-controlled current source, corresponding to the diode's conduction characteristics, in parallel with a nonlinear capacitance, corresponding to the junction capacitance of the diode. The parallel combination is in series with a "spreading resistance,"  $R_s$ , that models the loss behavior of the diode when it is strongly conducting.



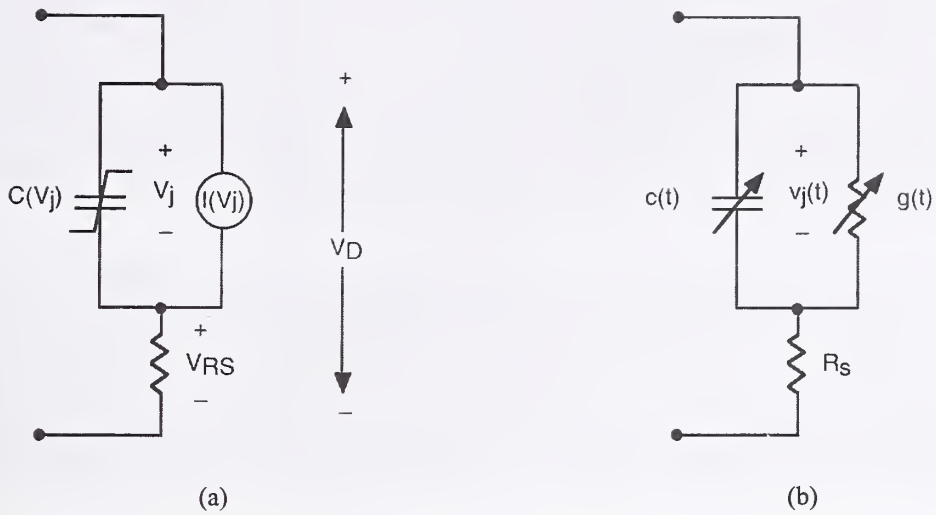


Figure 3-1. Models for a Schottky-barrier diode. (a) Large-signal model; (b) Small-signal model.

The large-signal forward-bias current through a Schottky-barrier diode can be expressed as [21, 22]

$$I(V_j) = I_s \left( \exp \left( \frac{qV_j}{nkT} \right) - 1 \right), \quad (3-1)$$

where  $V_j$  is the large-signal voltage across the diode junction (not including the voltage drop,  $V_{RS}$ , across the spreading resistance  $R_s$ ),  $I_s$  is the reverse saturation current,  $q$  is the charge on an electron ( $1.6 \times 10^{-19}$  C),  $n$  is the ideality factor,  $T$  is the junction temperature (K), and  $k$  is the Boltzmann constant ( $1.37 \times 10^{-23}$  J/K). Equation (3-1) is valid for  $V_D$  greater than  $-5nkT/q$ , where the diode is mildly reverse biased. SPICE utilizes other equations for the strong reverse-bias and breakdown regions of the diode [22]. The junction capacitance is given by

$$C_j(V_j) = \frac{C_{j0}}{\left( 1 - \frac{V_j(t)}{\phi_{bi}} \right)^\gamma}, \quad (3-2)$$

where  $C_{j0}$  is the zero-bias junction capacitance. (Note that  $C_j = C_{j0}$ , a constant, when  $V_j = 0$ .) This is an important concept in our nose-to-nose error calculations),  $\phi_{bi}$  is the junction's built-in potential, and  $\gamma$  is the grading coefficient ( $\gamma = 0.5$  for Schottky-barrier diodes and for linearly graded junction in  $pn$ -type diodes [23]). We define the large-signal junction capacitance as an incremental quantity  $C(V_j) = dQ_d/dV_j$ , after Maas [21]. This definition offers consistency with the large- and small-signal definitions of the conductive branch of the diode, where a large-signal conductance  $I/V$  is not typically defined.

Two other parameters typically included in SPICE diode models and not defined above are the transit time,  $\tau_t$ , and the energy gap,  $E_G$ . The transit time is the average time for minority carriers to travel through the narrow region of a short-base diode [22]. It is typically set to zero in SPICE Schottky-diode models since there is essentially no minority-carrier transport. The energy gap is used in SPICE to differentiate between different types of diodes, such as silicon, germanium, and Schottky-barrier diodes. The value for Schottky diodes in SPICE is typically 0.69 eV [22].

The values of  $I(V_j)$  and  $C(V_j)$  are determined by the internal constants of the diode ( $R_s$ ,  $n$ ,  $I_s$ ,  $\phi_{bi}$ , and  $\gamma$ ) and by the instantaneous large-signal junction voltage,  $V_j$ , and the junction temperature  $T$ . In our sampling circuit, the value of  $V_j$  at any moment in time depends primarily on the large-signal excitation (the strobe pulse) and the surrounding electrical network. Through network analysis, SPICE determines  $V_j$  as a function of time, and from this, the large signal response  $I(V_j)$  and  $C(V_j)$ , both of which are time-varying functions.

Figure 3-2 shows a typical example of the change in junction capacitance over time as the strobe fires across the sampling diodes in our SPICE sampling-circuit model. We increase the diode's grading coefficient,  $\gamma$ , from zero (solid flat line) to 0.9 (line with greatest variation). The grading coefficient  $\gamma = 0.5$  corresponds to a typical Schottky-barrier diode, as mentioned above. The upper and lower bounds of  $\gamma = 0$  and  $\gamma = 0.9$  are included for illustrative purposes only. The case  $\gamma = 0$  is a nonphysical case where the diode's junction capacitance is constant.  $C_{j0}$  in this example is 0.045 pF, the value of the flat line. We see that the maximum instantaneous  $C_j$  increases to more than twice its original value when  $\gamma = 0.5$ .

### 3.1.2 Small-Signal Model

The model in Fig. 3-1(b) is employed when the sampler is responding to a small-signal input. In this case, the diode junction is represented as a time-varying conductance in parallel with a time-varying capacitance. The conductance and the capacitance vary as linear functions of time. The values of  $g(t)$  and  $c(t)$  are set by the time-varying large-signal junction voltage. A small-signal input voltage,  $v_D(t)$ , will not alter their values, but will respond to them as to any time-varying, linear circuit element [21].

The diode's small-signal voltage and current can be related by [15, 21]

$$i_d(t) = g(t)v_j(t) + \frac{dq_j(t)}{dt} \quad (3-3 \text{ (a)})$$

$$= g(t)v_j(t) + \frac{dC(t)v_j(t)}{dt} \quad (3-3 \text{ (b)})$$

$$= g(t)v_j(t) + C(t)\frac{dv_j(t)}{dt} + v_j(t)\frac{dC(t)}{dt}, \quad (3-3 \text{ (c)})$$

where  $q_j(t)$ , the small-signal charge stored in the diode's junction capacitance, is  $C(t)v_j(t)$ .

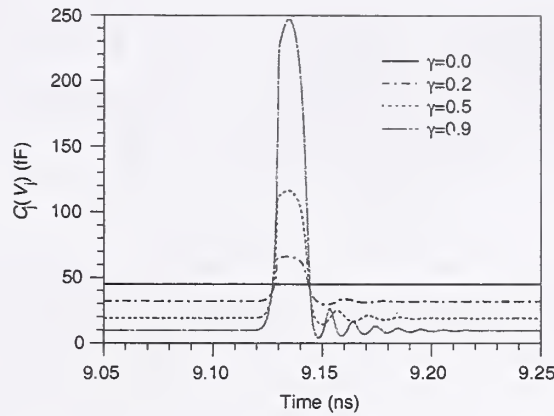


Figure 3-2. Sampling diodes' junction capacitance  $C(V_j)$  for various values of grading coefficient,  $\gamma$ , as the strobe fires.

Calculating these small-signal quantities from our SPICE simulations is made difficult by the fact that SPICE provides us with only  $V_D$ , the total large-signal voltage across the diode (see Fig. 3-1(a)), and  $I_D$ , the total current through the diode. To find  $V_j$  (refer to Fig. 3-1), we first calculated  $V_{RS}$ , the voltage across the spreading resistance, as the product of  $I_D$  and  $R_s$ . We then subtracted  $V_{RS}$  from  $V_D$  to get  $V_j$ . We found  $I(V_j)$ , the current in the non-capacitive branch of the large-signal model of Fig. 3-1, using eq (3-1). At this point we were able to determine the small-signal conductance  $g(t) = dI(V_j(t))/dV_j(t)$ . The small-signal capacitance was found from eq (3-2).

We found the small-signal junction voltage in the diode by subtracting two values of  $V_j$  from SPICE simulations with and without a small-signal input applied to the sampling circuit. The range of values for a "small-signal" input will be defined in Section 4.3.3. With the small-signal junction voltage, the conductance, and the capacitance

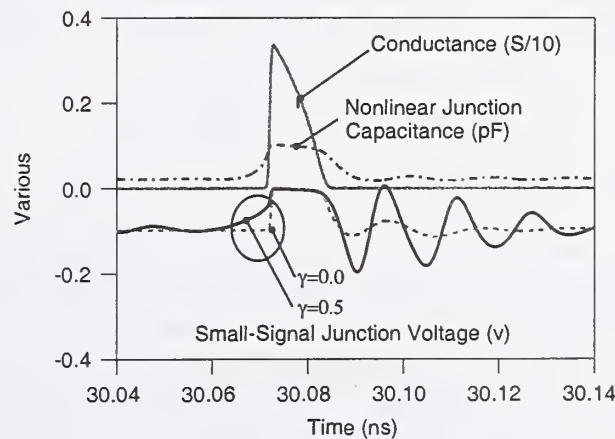
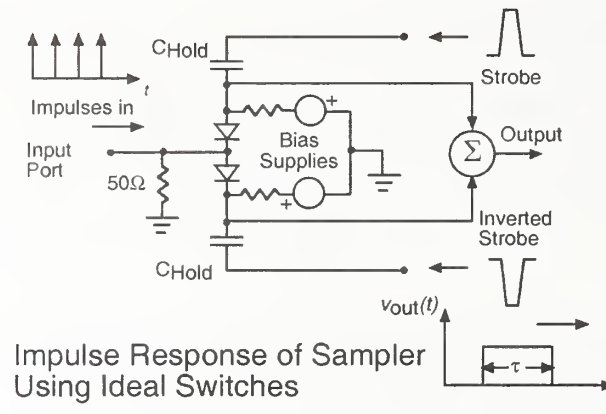
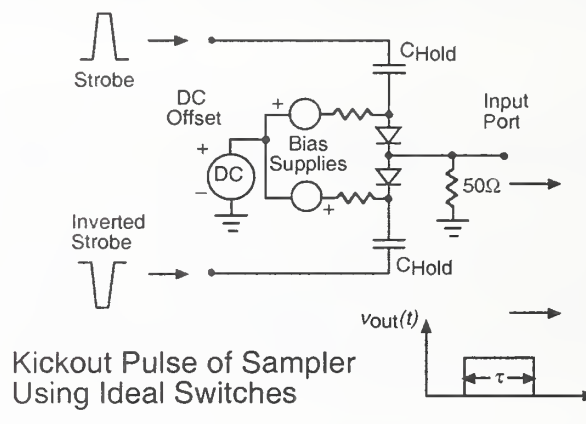


Figure 3-3. Small-signal junction voltage with (solid) and without (dashed) nonlinear capacitance included in the SPICE model. Also shown are the diode conductance (dots) and junction capacitance (dash-dots). For the case with  $\gamma = 0.0$ , the junction capacitance (not shown) is a constant  $C_{j0} = 0.045$  pF. The ringing in the curves is due to the presence of inductive packaging parasitics, not used in the default sampling-circuit model described in Section 4.



(a)



(b)

Figure 3-4. (a) Impulse response and (b) kickout pulse generation for a simple two-diode sampler.

known, we could then find the small-signal current through the diode. Typical small-signal values are plotted in Fig. 3-3. Knowledge of the small-signal response can help us understand potential errors in the nose-to-nose calibration caused by the diode's asymmetric conductance and nonlinear junction capacitance.

### 3.2 Diode-Related Errors in the Nose-to-Nose Calibration

To illustrate the effect that the asymmetry in the diode conductance function and nonlinear diode junction capacitance have on the nose-to-nose calibration, we will first examine a nearly ideal case in which we replace the sampling diodes by ideal switches. We define an ideal switch as one with infinitely short turn-on and turn-off times, but which stays on for a finite period. Thus, the conductance of the switch is a rectangular function of time with a width corresponding to the duration of its closure (This pulse is rectangular when the RC time constant of the circuit resistance and the hold capacitor is much longer than the period of the sampling window. This condition is true for the sampling circuits we investigated.). Because the sampling circuit will respond to any input signal that arrives while the switch is shut, but will not respond to its input when the switch is open, the impulse response has the same shape as the switch-closure conductance function.



We can explain this in terms of sampling-circuit operation as follows: if a pulse train of Dirac delta functions is used as excitation to the sampling circuit, the impulse response may be measured directly. The sampling circuit will respond to the delta functions only when the switch is closed, allowing the hold capacitors to charge, as shown at the bottom of Fig. 3-4(a). The impulse response will be traced out after many sampling cycles.

We generate kickout pulses on a second ideal-switch sampler by replacing the impulse excitation with a DC offset on the bias lines. Each time the strobe fires, a pulse of the same duration as the switch closure appears at the input port of the sampler, as shown at the bottom of Fig. 3-4(b). Again, the kick-out corresponds to the response of the switch as it closes, allows current to flow, and then opens.

If we now connect the input ports of our two ideal-switch samplers nose-to-nose, the output will be the convolution of the rectangular kickout and the rectangular impulse response. This convolution, a triangular waveform of duration  $2\tau$ , is what we would measure at the output of the second sampler. A simple deconvolution process gives us  $\tau$ , from which we can find the impulse response.

When the ideal switches are replaced by diodes, the impulse response is no longer a simple rectangular function, but is altered by both the conductance and the junction capacitance of the diodes, as shown in the right-hand curves of the simulation results presented in Fig. 3-5. The left-hand curves in this figure illustrate the additional effect the nonlinear diode junction capacitance has on the kickout pulse. We see that the kickout pulse rise and fall times are affected by the increase in nonlinear capacitance, while there is only a minimal change in the impulse response. This broadening of the kickout pulse can be explained by considering the components of the small-signal current in the sampling diodes.

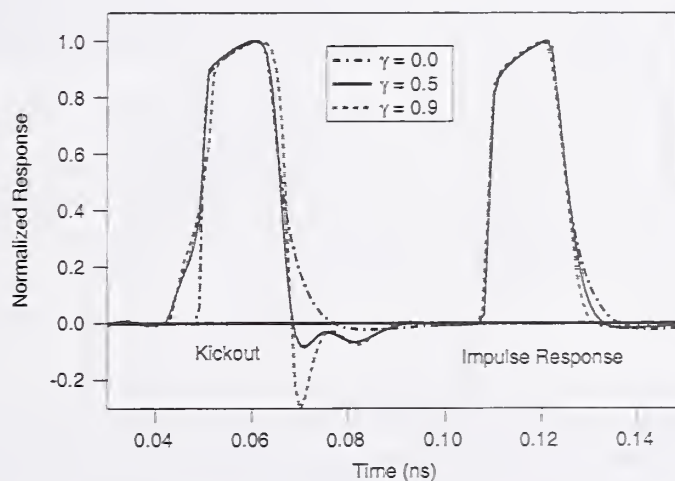


Figure 3-5. Kickout pulse and impulse response for increasing nonlinearity of diode junction capacitance. The impulse response has been shifted in time for clarity. Offset voltage is 0.1 V DC.



### 3.2.1 Diode Conductance

Asymmetry in the sampling diodes' conductance function can significantly alter the shape of the kickout pulse compared to that of the impulse response [15], due to the "time reversal" of the impulse response described in Ref. [3]. This, in turn, can lead to errors in the nose-to-nose calibration [2, 3, 14]. Using the technique described above, we plot the time-varying conductance function of the sampling diodes in Fig. 3-6. We see that the conductance is indeed an asymmetric function of time.

However, because the strobe pulse turns the diodes on quickly, the transition from a conductance value of 0 S (corresponding to an infinite impedance) to a value greater than 1 S (corresponding to an impedance less than 1  $\Omega$ ) is very rapid, approximately one or two picoseconds. The shape of the conductance function above 1 S will not significantly affect the loading of the sampling circuit. Thus, the effect of the conductance asymmetry on the error in the nose-to-nose calibration is minimal. This is demonstrated in Section 5, where we examine the phase error in the nose-to-nose calibration with a constant, non-time-varying diode junction capacitance (see Fig. 5-3). The remaining error is due to the time-varying diode conductance and, potentially, other effects, but we see that this phase error is minimal.

### 3.2.2 Nonlinear Diode Junction Capacitance

The influence of the sampling diodes' nonlinear junction capacitance on the phase error in the nose-to-nose calibration is illustrated in Fig. 3-3, which shows simulation results for the kickout sampler configuration with  $V_{\text{offset}} = 0.1$  V. Shown are the small-signal junction voltage,  $v_j(t)$ , with nonlinear junction capacitance ( $\gamma = 0.5$ , solid curve) and with constant junction capacitance ( $\gamma = 0.0$ , dashed curve). Also shown are the diode conductance and junction capacitance. Recall that the case with constant diode junction capacitance is nonphysical. For the constant capacitance case,  $v_j(t)$  changes only when the diode starts to conduct, as shown in the highlighted area of Fig. 3-3. For the case with  $\gamma = 0.5$ ,  $v_j(t)$  follows the nonlinear capacitance curve. As indicated by the last two terms in eq

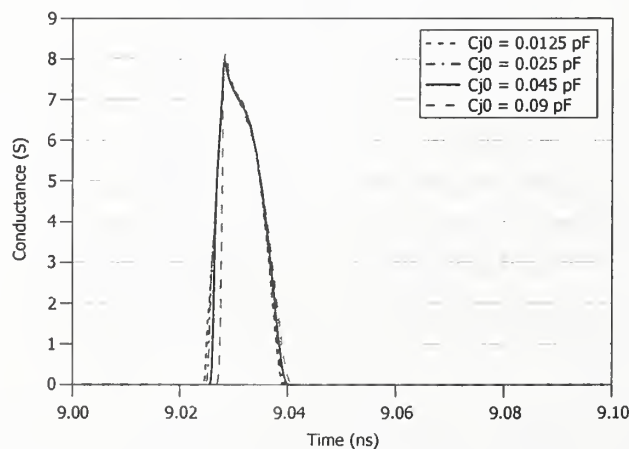


Figure 3-6. Diode conductance function for one of the two sampling-circuit diodes calculated from SPICE simulations for four different values of diode junction capacitance.

(3-3(c)), the time-varying quantities  $C(t)$  and  $v_j(t)$  give rise to a small-signal displacement current. This current causes the kickout pulse to broaden with nonlinear junction capacitance [20].

The reason that the impulse response does not broaden can be understood by realizing that the kickout is proportional to the instantaneous charge on the hold capacitors, while the impulse response is reconstructed from digitized samples, each of which is generated over one complete sampling cycle. The net charge transferred to the hold capacitors through the diode capacitance over one complete sampling cycle must be zero, since no conduction current path exists through the diode capacitance [15].

Following this introduction to the large- and small-signal diode models and the effects of the nonlinear junction capacitance on the nose-to-nose calibration, we will introduce the SPICE model in Section 4 that we then used in the parametric studies of Section 5. SPICE utilizes the large-signal diode model of Fig. 3-1(a), and the corresponding equations for large-signal current and diode capacitance given in eqs (3-1) and (3-2), respectively.

#### 4. SPICE Simulations

We used SPICE simulations to parametrically study the effects of varying the values of sampling-circuitry components on the nose-to-nose calibration phase error. SPICE is a circuit simulator that uses time-domain differential equations to represent circuit element input/output relationships. Circuit elements are linked through common nodes, and network analysis is used to solve the resulting system of equations. As we will see, SPICE offers a high degree of accuracy in the analysis of circuits for which well-established analytic models exist.

We have two primary goals for our SPICE model of the sampling circuitry: Firstly, we want to simulate the behavior of real samplers used in nose-to-nose calibrations. We do this by developing a model of the sampling circuit whose nose-to-nose derived impulse response compares well to measurements. When our simulated results are similar to measured results, we expect that our estimate of the contribution of the sampling circuitry to the total phase error is at least of the same order as the contribution of physical samplers. As a result, we expect that our parametric studies will demonstrate realistic sensitivity to variation in component values. The second goal for our SPICE model is that it be robust enough for parametric study over a wide range of component values.

In this section, we consider sampling-circuit models derived from two independent sources. We compare the nose-to-nose-derived impulse response of these models to nose-to-nose measurements and to each other. We synthesize a “default” SPICE model from these and then study convergence to determine the range of valid simulation conditions, such as time step and sampling rate, for this particular model. In the end, we will have developed a default nose-to-nose simulation that is robust enough to accurately perform numerical experiments for a broad range of parametric studies.

## 4.1 SPICE Models

Both sampler models that we considered are based on sampling circuits with 20 GHz input bandwidths and are of the two-branch balanced type shown in Fig. 4-1. The first was described in a 1982 paper by Sedki Riad [19]. This older-style sampling circuit used discrete components, and so the model includes diode packaging parasitics. The second model was provided by John Kerley [24], one of the authors on the seminal nose-to-nose work [1]. This model incorporates a monolithic diode structure similar to that found in samplers used in the type of oscilloscope we desire to calibrate using the nose-to-nose procedure.

The two sampler models have a similar layout, with a balanced diode configuration in which the strobe pulse cancels at both the input and output ports (although in practice the cancellation is not perfect). The strobe source for these samplers uses a step generator that drives a shorted transmission line in parallel with the sampling diode circuitry (see Fig. 4-1). A sharp voltage step initially turns the sampling diodes on. Reflection of the step from the shorted end of the transmission line turns the diodes off at  $2\tau_d$ , where  $\tau_d$  is the transmission line delay. We used a two-section ladder network to implement the transmission line in SPICE. We describe the models of Riad and Kerley in detail below, highlighting the features that we incorporated into our default sampling-circuit model. A table summarizing sampler model component values is provided at the end of Section 4.2.

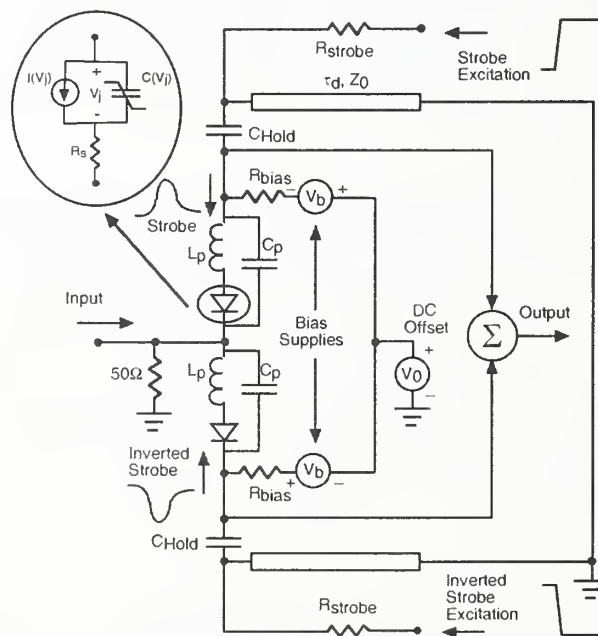


Figure 4-1. Schematic of the type of two-branch sampling circuit used in nose-to-nose measurements and in our SPICE simulations. The inset shows the large-signal equivalent circuit of the sampling diode.



#### 4.1.1 Riad's Model

Riad [19] developed an equivalent-circuit based model of a sampling head that used discrete, packaged sampling diodes. Model parameters were extracted from dimensional and electrical measurements made on subsections of a disassembled sampling head. Refer to Fig. 4-1 for definitions of components described below. Because this model is simple and straightforward to implement, we used many of its features in our default SPICE model.

Riad specified a reverse bias voltage,  $V_b$ , of 1.63 V and bias resistors,  $R_{bias}$ , of 3600  $\Omega$ . The strobe source step generator for this model has a source impedance of approximately 57  $\Omega$ , driving an 85.2  $\Omega$  transmission line that is shorted at its far end. We used a transmission line delay,  $\tau_d$ , of 7 ps in our default SPICE model (this value was not given in Riad's paper). The strobe generator amplitude was specified as 12 V in Riad's paper. We implemented this in SPICE by applying 6 V in each branch to give a differential strobe pulse of 12 V total amplitude. The strobe inputs are labeled "Strobe" and "Inverted Strobe" in Fig. 4-1. The simplified output circuit consists of a charge amplifier that sums the charge stored on the hold capacitors during each sampling cycle. The value of the hold capacitor,  $C_{hold}$ , was not given, so we used a value of 4 pF in our default model. Our 4 pF hold capacitor combined with the 50  $\Omega$  input impedance yields a 200 ps RC time constant, much longer than the 10 ps or so aperture time during which the diodes are forward biased. This means the hold capacitor essentially looks like a short circuit for the duration of the sampling aperture and thus the hold capacitor's response will not affect the sampled data, as desired.

Several important diode circuit parameters derived from measurements were given in Riad's paper. These parameters are used in eqs (3-1) and (3-2), and include the spreading resistance,  $R_s$ , the zero-bias junction capacitance,  $C_{j0}$ , and the reverse saturation current,  $I_s$ . We used these values directly in our default SPICE model. For other diode parameters in our SPICE model, we used values for typical Schottky-barrier diodes from Ref. [21] or [22], including a minority carrier transit time,  $\tau_t$ , of zero. These values are summarized in Table 4-1 at the end of this section. Because discrete diode structures are used in the sampling circuitry, packaging parasitics are included in the sampler circuit, given by  $C_p$  and  $L_p$  in Fig. 4-1.

#### 4.1.2 Kerley's Model

This model was based on a SPICE simulation of a sampler with a 20 GHz input bandwidth that was conducted by Kerley in 1991 [24]. This sampler is similar to the 50 GHz-input-bandwidth sampling head oscilloscope plug-ins used in nose-to-nose calibrations today [2, 5]. Thus, we expect this model to approximate nose-to-nose measurements better than the Riad model, at least to the upper frequency of 20 GHz that we use in this study.

Kerley's model is similar to the Riad model with the primary difference in the bias circuitry, where the bias resistor was replaced with a series combination of a resistor

and an inductor, chosen empirically to match measurement. Other differences include: a lower bias supply voltage in the Kerley model, a higher impedance for the shorted transmission line used for strobe-pulse shaping, and a somewhat longer delay time for this transmission line. The hold capacitors were 2 pF [2]. Because the sampler utilized a monolithic diode structure, packaging parasitics  $C_p$  and  $L_p$  were presumed negligible and were not included in the model. The strobe drive circuit for this model was complicated, with filtering added to reproduce the strobe pulse observed in this type of oscilloscope.

Kerley used three diode model configurations in his experiments, as shown in Fig. 4-2. One used the standard SPICE nonlinear junction capacitance model [see eq (3-2)], with a zero-bias junction capacitance,  $C_{j0}$ , of 40 fF (from the manufacturer). The second, for investigation of the effects of nonlinear capacitance on the nose-to-nose calibration, used a constant junction capacitance [ $C(V_j) = \text{constant}$ ] of 40 fF. The third model split the junction capacitance between a branch with a fixed value of 15 fF and a branch that included the nonlinear junction capacitance with  $C_{j0} = 25$  fF [see Fig. 4-2(c)]. In his notes [24], Kerley stated that the third one is probably the most accurate representation of the diode, based on the manufacturer's information. In each Kerley diode model, only the reverse saturation current  $I_s$  and the spreading resistance,  $R_s$ , were specified, again based on the manufacturer's specifications. He left the other diode parameters as the SPICE default [22]. These values are summarized in Table 4-1 at the end of Section 4.2.

#### 4.2 Development of the Default Sampling-Circuit Model

As mentioned above, we had two primary considerations in developing our default sampling-circuit model: that the model approximate measurements of a nose-to-nose derived impulse response well, and that the model be robust enough for parametric study. We begin by comparing nose-to-nose measurements with the Kerley model. Results are shown in Fig. 4-3. In this comparison we used the Kerley model rather than

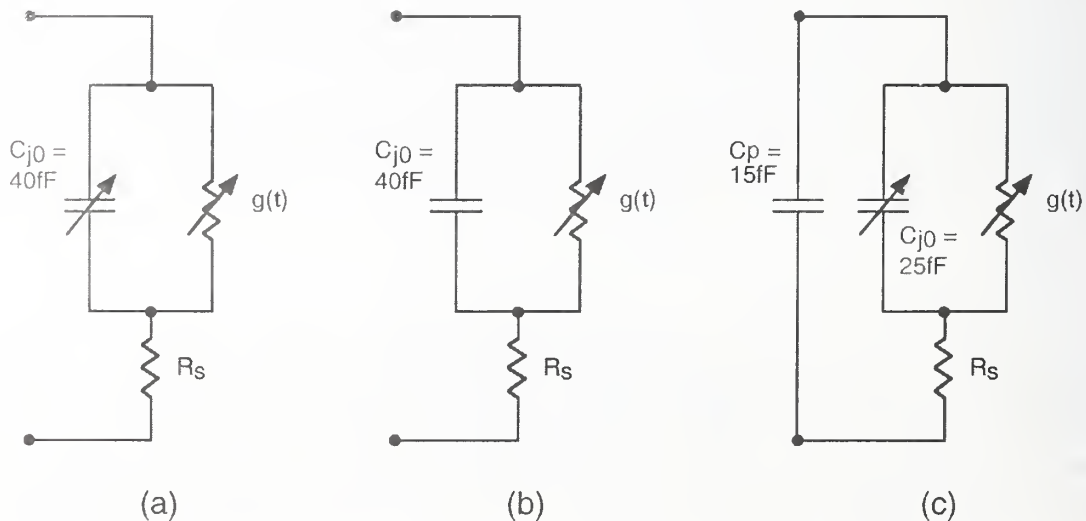


Figure 4-2. Three diode models used by Kerley in SPICE simulations: (a) standard diode model with nonlinear junction capacitance, (b) constant junction capacitance equal to the zero-bias junction capacitance, (c) split-diode model with 15 fF of constant capacitance and 25 fF of nonlinear capacitance.



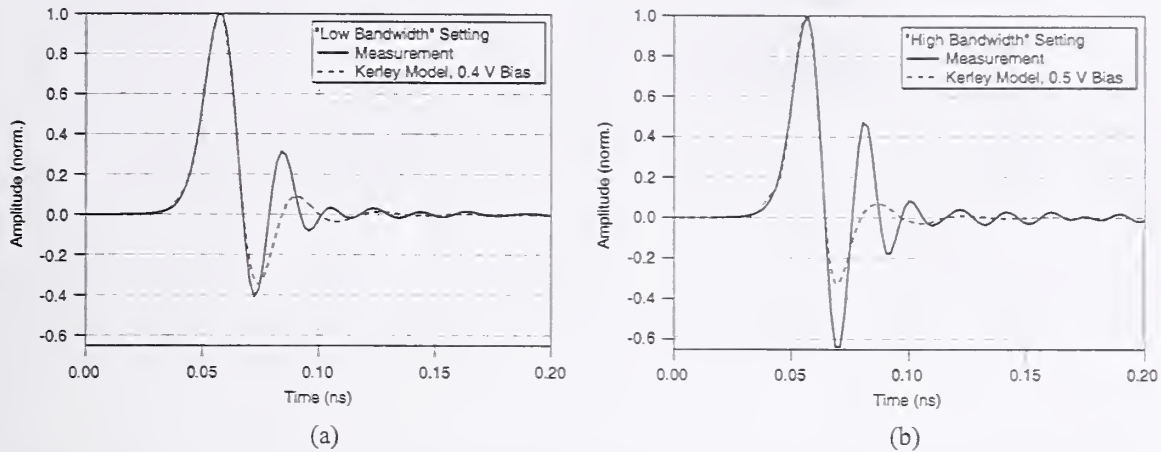


Figure 4-3. Comparison between nose-to-nose measurements and simulations using the Kerley sampling circuit SPICE model. (a) Low bandwidth setting, corresponding to a measured upper input frequency of 20 GHz for the oscilloscope; (b) High bandwidth setting, corresponding to a measured upper input frequency of 50 GHz. The bandwidth setting changes the reverse bias on the sampling diodes.

the Riad model since we believe it is essentially the same circuit used in nose-to-nose measurements, but with an input bandwidth of 20 GHz rather than 50 GHz.

The solid curves in Figs. 4-3(a) and (b) plot the output time responses of two oscilloscopes connected in the nose-to-nose configuration and are approximately equal to the convolution of the kickout pulse emanating from the first oscilloscope and impulse response of the second oscilloscope (see Section 2.4). The “Low” and “High” bandwidth settings on the oscilloscopes set the input bandwidth by changing the reverse bias on the diodes. The Low bandwidth setting corresponds to an RF measurement input bandwidth of 20 GHz, and the High bandwidth setting corresponds to a measured input bandwidth of 50 GHz. The curves were generated from measurements made at NIST and have been corrected for time-base distortion and impedance mismatches between samplers due to external connectors and cables [5]. The dashed curves in Fig. 4-3 correspond to our SPICE nose-to-nose simulation using the Kerley model with values of bias voltage chosen by comparison to measurement. Because an ideal isolation network connects the output of one sampler to the input of a second sampler, mismatch correction is not necessary in these simulations.

The measurement and simulation do not match precisely, nor should they. The measurements include effects of additional unknown filtering internal to the oscilloscope, but external to the sampling circuitry, not represented in the models. However, the similarity of the curves in Figs. 4-3(a) and (b) give us an indication that our SPICE circuit configuration is ostensibly correct and that its model parameters are, at least, of the same order as those found in real sampling circuits. Having addressed the issue of model and measurement comparability, we next turn to the issue of developing a robust model suitable for parametric study.

Figure 4-4 compares the Riad model to the Kerley model. For best comparison, we use the same strobe pulse conditions in the two models, the Kerley diode model

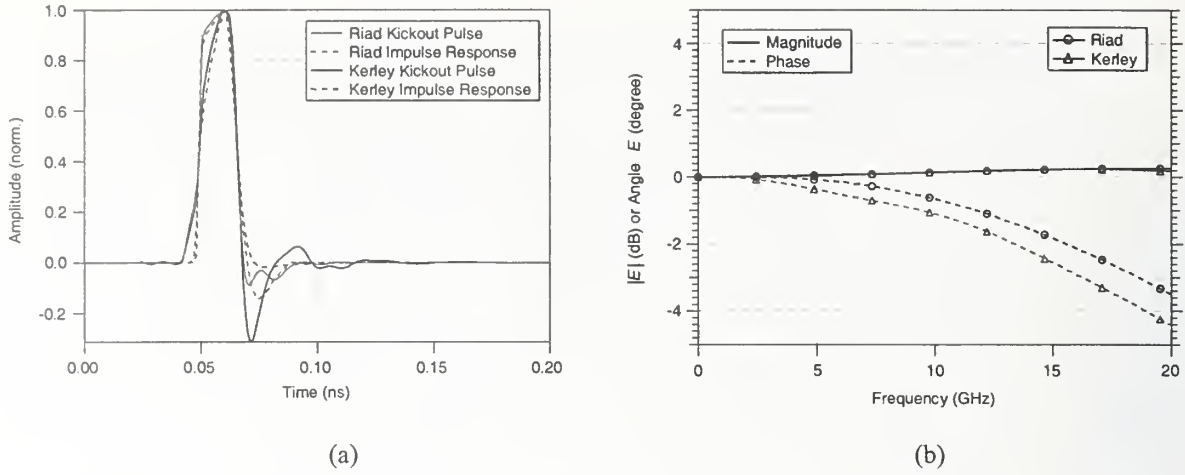


Figure 4-4. Comparison of the Riad and Kerley sampling circuits. (a) Time-domain representation of kickout pulses and impulse responses. (b) Frequency-domain magnitude and phase of the correction factor  $E(f)$  for the two models. The Riad circuit has no packaging parasitics and a strobe pulse with a shorter, 10 ps rise time to better emulate modern samplers. We used a strobe-shaping transmission-line delay of  $\tau_D$  is 7 ps for the Riad sampler and 8 ps for the Kerley sampler.

shown in Fig. 4-2(a) (since this diode model is most similar to the Riad diode model), and the Riad model without packaging parasitics, to best approximate the monolithic structure of Kerley's circuit. We compare simulation results for the kickout pulse and impulse response in Fig. 4-4(a). In Fig. 4-4(b), we plot the frequency-domain correction factor,  $E(f)$ , which tells us how similar the nose-to-nose-derived impulse estimate is to the true impulse response (see Section 2.4). The dashed curve indicates the error in the phase component of the nose-to-nose-derived impulse response when compared to the true impulse response. Figure 4-4(b) shows that even though the results of the Riad and Kerley models are not identical, they are similar, with approximately  $1^\circ$  difference between them in the phase component of the correction factor at 20 GHz.

While Fig. 4-4 shows that the two models give similar results, Fig. 4-3 shows that the Kerley model agrees well with measurement. However, the Kerley sampler is difficult to simulate because inductors are used in the bias lines. The discharge time for these inductors is quite long, making the simulation touchy and extremely long. Because we require a robust model capable of performing over a wide parameter space, for the remainder of this work we define our "default" sampling circuit as the basic configuration of the Riad sampler, with two important modifications. First, we do not include the packaging parasitics, to better approximate the monolithic diode structure of present-day samplers (discussed below in Section 4.2.1). Second, we use a strobe pulse whose rise time is faster than the 32 ps specified by Riad, to better approximate 50 GHz samplers currently used in nose-to-nose measurements. The decision on which strobe pulse rise time to use is detailed in Section 4.2.2. A summary of our default sampler's characteristics can be found in Table 4-1.

The magnitude and phase of  $E(f)$  were plotted in Fig. 2-7 for the default SPICE model of the sampler. For the default sampling-circuit configuration that we examined, our default magnitude error was approximately 0.25 dB, which is lower than the  $\sim 0.6$  dB difference between a swept-sine and a nose-to-nose calibrated oscilloscope impulse response measured in Ref. [5]. Our default phase error was approximately  $3.3^\circ$  at 20

Table 4-1. Parameters of the two models discussed above and our default sampling circuit model.

	Diode parameters								Circuit parameters				
	$R_s$ ( $\Omega$ )	$I_s$ (pA)	$n$	$C_{j0}$ (fF)	$\phi_{bi}$ (V)	$\gamma$	$E_G$ (eV)	$C_H$ (pF)	$V_{bias}$ (V)	$R_{bias}$ ( $\Omega$ )	Strobe (V)	Strobe rise (ps)	Pack- aging (pF/nH)
Riad model	19	26.7	1.08	45	0.7	0.5	0.69	4.0	1.63	3600	12	32	15/8
Kerley model	10	0.03	1.0	40	1.0	0.5	1.11	2.0	lower	R+L	~10	~20	--
Default model	19	26.7	1.08	45	0.7	0.5	0.69	4.0	1.63	3600	12	10	--

GHz. This is of the order of the phase difference between an EOS measurement and a nose-to-nose calibrated oscilloscope measurement given in Ref. [9]. These differences between measured results and our sampling circuit are reasonable, since the measurements involved complete oscilloscopes and our model only approximates the sampling circuitry.

#### 4.2.1 Packaging Parasitics

Figures 4-5(a) and (b) show the change in both the magnitude and phase of the correction factor,  $E(f)$ , for three different values of diode grading coefficient,  $\gamma$  (defined in Section 3.1.1). We see a significant change in the phase component of  $E(f)$  with and without packaging parasitics included in the model, especially for  $\gamma = 0.5$ , the value for Schottky diodes. To better approximate the monolithic diode circuit of present-day samplers, our default model does not include packaging parasitics.

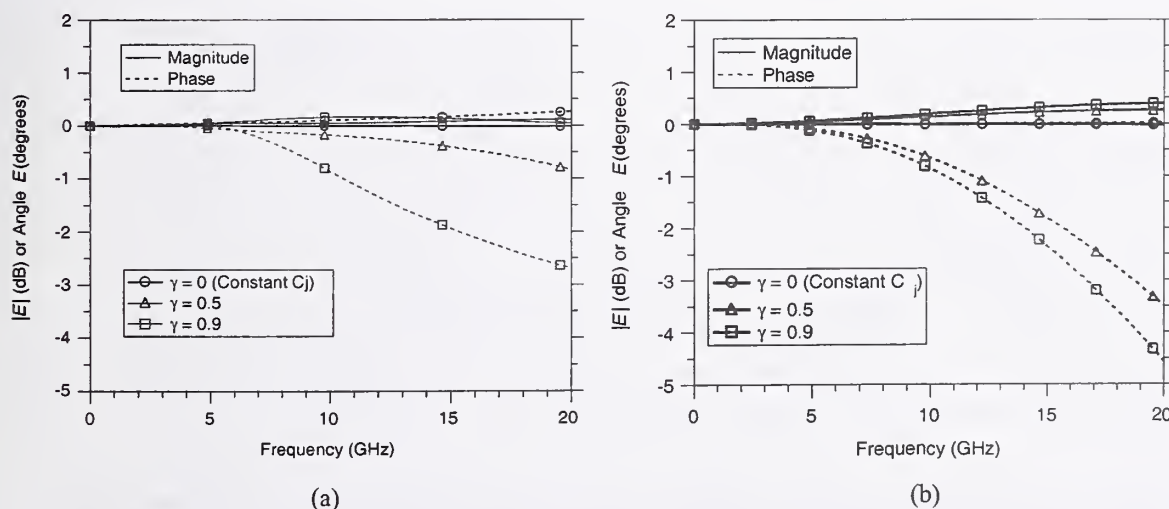


Figure 4-5. Results from SPICE simulations of Riad's sampler model: (a) with, and (b) without packaging parasitics for three different values of diode grading coefficient,  $\gamma$ . Packaging is used in samplers consisting of discrete components, such as the Riad model shown in (a). To better approximate monolithic structures, packaging parasitics are neglected in (b).



## 4.2.2 Strobe-Excitation-Pulse Rise Time

As mentioned in Section 4.1, the strobe pulse in our simulations is generated when a step-pulse (approximated in SPICE by a long-duration trapezoidal pulse) is fed into a shorted transmission line (see Fig. 4-1). The reflection of this step-pulse from the shorted end turns the strobe off after twice the delay time of the transmission line. The rise time of the strobe-excitation pulse determines the strobe pulse rise time. The sharpness of the strobe's rising edge helps determine the bandwidth of the sampler. Our goal is to use an excitation-pulse rise time that gives a diode "aperture time" similar to the 10 ps specified in the literature [2]. The aperture time is the period during which the strobe forward-biases the sampling diodes causing them to conduct.

Figure 4-6(a) shows SPICE simulations of the strobe pulse of our default sampling circuit for four different excitation-pulse rise times (the rising edge of the step-pulse shown in Fig. 4-1): 5 ps, 10 ps, 15 ps, and 20 ps. The strobe pulse is measured from the hold capacitor/diode input node to ground, as shown in Fig. 4-1. Note that the strobe pulse itself is not trapezoidal because the excitation pulse is altered by the characteristics of the transmission line and the other impedances in the sampling circuit. In addition, the amplitude of the strobe pulse is much smaller than the 6 V of the trapezoidal excitation pulse, due to voltage drops elsewhere in the sampling circuit.

Figure 4-6(b) shows simulation results of the sampling diodes' small-signal junction voltage using the same excitation-pulse rise times as in Fig. 4-6(a). The small-signal junction voltage gives us an indication of the aperture time of the sampling circuit. During the aperture time, the diodes strongly conduct, their conductance is high, and the voltage drop across the diode,  $v_j$ , is near zero. In Fig. 4-6(b), excitation-pulse rise times

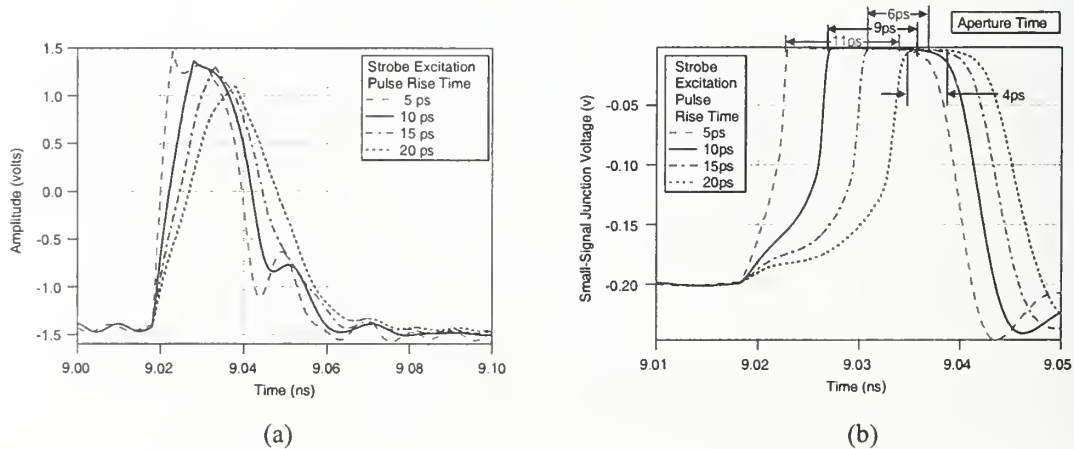


Figure 4-6. Simulations using our default sampling circuit model with several different strobe-excitation-pulse rise-times. (a) Strobe pulse (measured from the sampling diode input to ground). (b) Small-signal junction voltage across the sampling diodes. The legend corresponds to the excitation pulse's rise-time, and the markings at the top are the approximate aperture times. Note the decreased aperture time and the increased leading edge of the small-signal junction voltage for increasing excitation-pulse rise-times.



are given in the legend and approximate aperture times are indicated at the top of the plot. We see that the strobe with the 10 ps excitation-pulse rise time gives an aperture time of approximately 9 ps. Because the 50 GHz oscilloscope used in nose-to-nose measurements is reported to have a 10 ps aperture time [2], we choose a 10 ps rise time for the strobe excitation pulse. Note that we could also have chosen the 5 ps rise-time excitation pulse (corresponding to an 11 ps aperture time).

Figure 4-6(b) shows an interesting effect: as the strobe-excitation-pulse rise time increases (corresponding to a less-steep strobe pulse leading edge), the rise time of the small-signal junction voltage also increases. This effect can be explained by considering the parallel branches of the diode model, shown in the inset of Fig. 4-1. One branch corresponds to a conduction path, and the other to a charge displacement path through the diode junction capacitance. Charge builds up on the diode junction for a longer time before the diode actually conducts for strobe pulses with longer rise times. The resulting displacement current induces the longer leading edge in the small-signal junction voltage. As discussed in Section 3.2, the longer the leading edge, the greater the phase error in the nose-to-nose calibration. The amount of this phase-error increase is quantified in a parametric study in Section 5-3-2.

### 4.3 SPICE Simulation Convergence Studies

Using our default sampling-circuit model, we next synthesized a set of default SPICE simulation settings to use in our parametric studies of the nose-to-nose calibration procedure. We did this by checking simulation convergence with various simulation settings. In these convergence studies, we determined simulation settings that allow us to accurately resolve important characteristics of the sampling-circuit behavior while maintaining the highest computational efficiency possible. Specifically, our convergence studies involve:

1. Time step ( $t_{\text{step}}$ ): ensuring we use a sufficiently small time step to capture features in the nose-to-nose response to the highest frequency of interest (20 GHz in the present work).
2. Sampling cycle period ( $t_{\text{samp}}$ ): ensuring that our sampling period—the periodicity of the strobe firing—is long enough to keep the output of one sampling cycle from affecting the output of subsequent sampling cycles.
3. Input voltage level ( $v_{\text{in}}$ ): ensuring that the input signal amplitudes are small enough to be operating in the small-signal regime (where the kickout pulse and impulse response are not affected by the input amplitude).
4. Input pulse width ( $t_{\text{pw}}$ ): ensuring that our finite-duration input pulses can be accurately deconvolved from the output signal to generate a valid impulse response estimate.

Figure 4-7 shows how each of the items enumerated above is defined in the context of impulse-response generation, where we sample short-duration pulses whose period is slightly different from that of the strobe period. The short-duration pulses are deconvolved from the output signal to give us an impulse response estimate. If we were able to input a pulse train of true Dirac delta functions, the deconvolution step would be unnecessary. Refer to Section 2.2 for more detail on this procedure. The settings  $t_{\text{samp}}$  and  $t_{\text{delay}}$  are chosen by the user so that the period of the input signal is slightly different from that of the sampling cycle (the time between strobe firings). This enables us to progressively sample the entire impulse response. Kickout pulse generation occurs each time the strobe fires when there is a DC offset between the sampler's two branches. This is a more straightforward process in terms of the simulation parameters listed above and is not illustrated above.

Note that SPICE uses several nonstandard definitions:  $t_{\text{step}}$  is defined as the *maximum* of a variable time step. SPICE uses a time step smaller than  $t_{\text{step}}$  to resolve rapidly changing features of a waveform (such as the pulses in Fig. 4-7), and uses  $t_{\text{step}}$  in the more slowly varying parts of the time record. The pulse width  $t_{\text{pw}}$  is defined as the width of the top of the trapezoidal input pulse, rather than the width at full-width, half-maximum of the pulse.

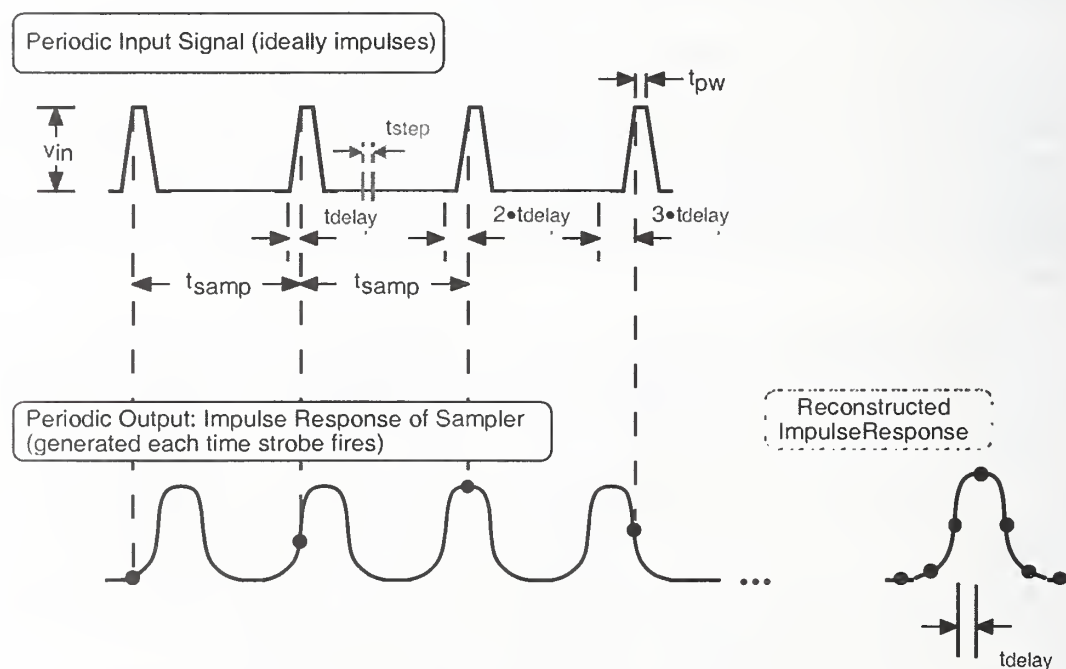


Figure 4-7. Definition of the simulation settings listed above and their role in generating the impulse response of the sampling circuit. When the period of the sampling cycle (given by  $t_{\text{samp}}$ ) is different from the period of the input signal, the increasing delay enables sampling of the entire impulse response of the sampler. Note that the periodic output consists of a convolution of the sampler's impulse response and the input pulse. When the input pulse is a Dirac delta function, no deconvolution of the input pulse is necessary.

### 4.3.1 Time Step

Figures 4-8(a) and (b) show kickout pulses and impulse responses, respectively, simulated using the Riad sampling-circuit model with three different maximum time steps ( $t_{\text{step}}$ ) in SPICE. See Table 4-1 for other circuit parameters, and Table 4-2 for other simulation settings. SPICE allows the user to set the maximum time step only, rather than a fixed time step, as mentioned above.

Figure 4-8(c) shows the magnitude and phase of the correction factor,  $E(f)$ , for nose-to-nose simulations using three values of  $t_{\text{step}}$ . We see that simulations with  $t_{\text{step}} = 0.5$  ps are very similar to those with a  $t_{\text{step}} = 0.25$  ps, but that an increase in both magnitude and phase error occurs when  $t_{\text{step}} = 1.0$  ps. Based on this result, we used either  $t_{\text{step}} = 0.5$  ps in simulations for samplers with identical, balanced diodes, or  $t_{\text{step}} = 0.25$  ps for samplers with a diode imbalance (see Section 5.4 for simulations of imbalanced diodes), where more detail was required for accurate simulations.

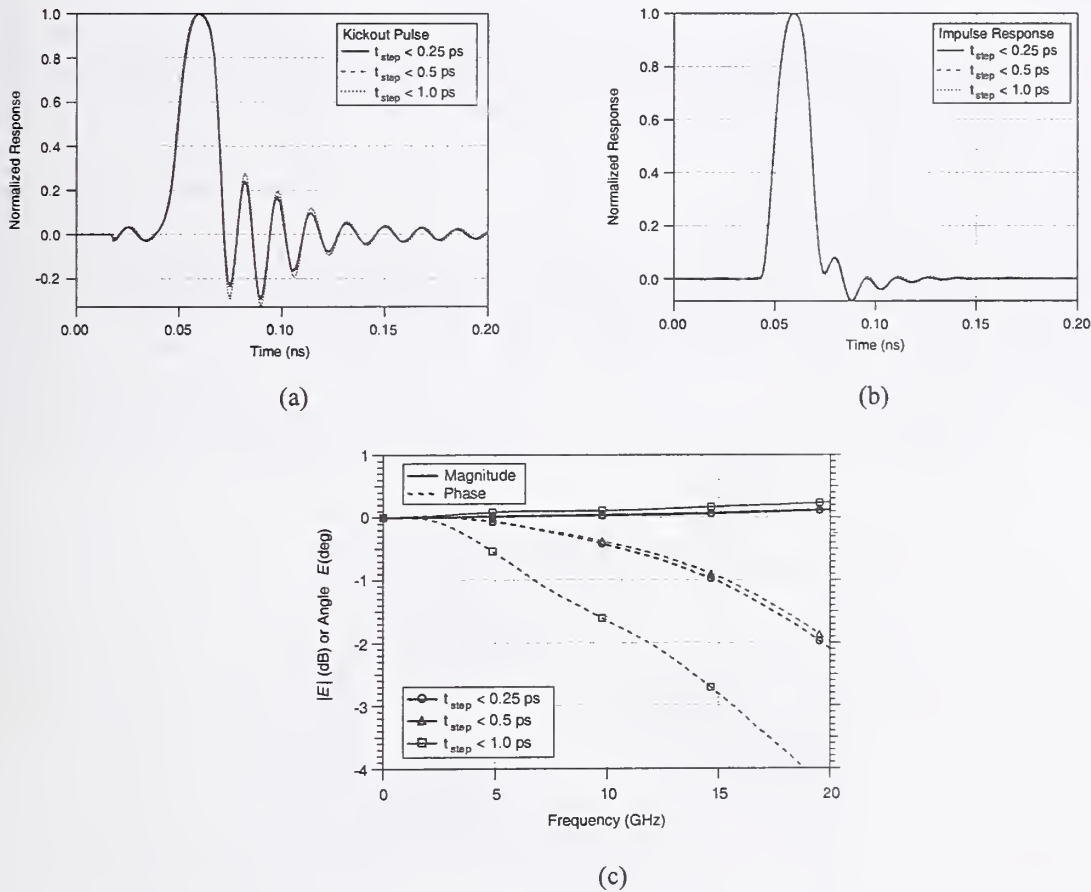


Figure 4-8. Results of nose-to-nose simulations using the Riad sampling-circuit model with three different maximum time steps in SPICE. (a) kickout pulses; (b) impulse responses; and (c) magnitude and phase of  $E(f)$ . Results for both magnitude and phase are similar for  $t_{\text{step}} = 0.25$  and  $0.5$  ps, but degradation is observed for  $t_{\text{step}} = 1.0$  ps.

### 4.3.2 Sampling-Cycle Period

The sampling-cycle period is the interval between strobe firings, and is called " $t_{\text{samp}}$ " in Fig. 4-7. One point in the reconstructed output signal is acquired each sampling cycle. For computational efficiency in the SPICE simulations, we would like to make the sampling-cycle period as short as possible. However, to ensure that charge stored from one sampling cycle doesn't affect the charge collected on subsequent sampling cycles, we must make the period long enough for the hold capacitors to fully discharge between strobe firings. This will give us the steady-state solution. In commercial oscilloscopes, a long delay, on the order of milliseconds, exists between samples. In our SPICE simulations, we hastened discharge by inserting switches across the hold capacitors and had them discharge the capacitors in a time frame that did not affect the accuracy of our sampling.

To make sure that our discharge switches performed properly, we ran several SPICE simulations with various sampling-cycle periods. Selected results are shown in Fig. 4-9, where we see obvious degradation in the correction factor when the sampling period is less than 400 ps. In this case the impulse response duration combined with the discharge switch closure time is not sufficient to allow proper discharge of the hold capacitor. The sample periods greater than 400 ps should theoretically be identical, but the effect of numerical error introduces differences in the phase-error calculations. We used a 500 ps sampling-cycle period for the simulations in this work since a 500 ps period gives greater computational efficiency than 750 ps or 1000 ps.

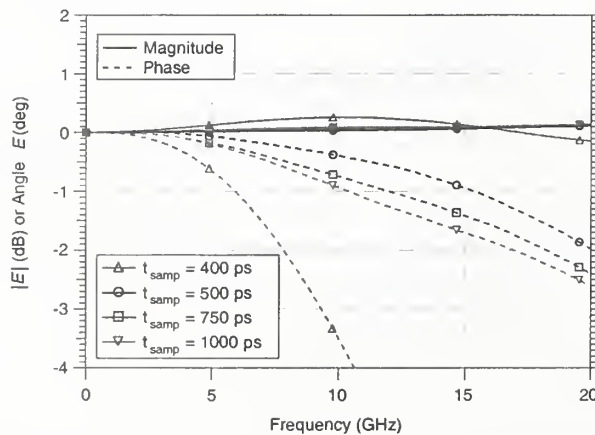


Figure 4-9. Magnitude and phase of  $E(f)$  calculated for four sampling-cycle periods: 400 ps, 500 ps, 750 ps, and 1000 ps. We see that the phase error increases for sampling periods both less than and (to a lesser extent) greater than 500 ps. A sampling-cycle period of 500 ps was chosen as our default in this work.



### 4.3.3 Input Voltage Level

One important premise of sampling-circuit operation is that the diode's large-signal behavior is not affected by the input signal. In the diode model we use, the large-signal strobe fixes the diode's conductance and junction capacitance, and ensures that the reconstructed response of the sampler to a small-signal input is linear. To calculate the impulse response and perform a simulation of the nose-to-nose calibration accurately, we must limit the input signal amplitude,  $v_{in}$ , so that the inputs to the sampler are in this small-signal regime.

We calculated the correction factor  $E(f)$  for various values of  $v_{in}$ , and present the results in Fig. 4-10. We see only minimal change in the magnitude and phase of  $E(f)$  for  $v_{in}$  less than 0.3 V. For this reason, we used an input level in subsequent simulations of 0.2 V (Note that measurements presented in Refs. [3] and [11] use a DC offset level of 0.1 V, and Ref. [13] states that the offset level must be less than 0.25 V for small-signal operation.). This input refers to either the peak amplitude of the pulses in the pulse train used for impulse response calculations ( $v_{in}$  in Fig. 4-7), or the DC voltage offset used for kickout generation. Even though kickout pulse and impulse response generation are two different effects, the small-signal requirement is satisfied for both with  $v_{in} = 0.2$  V.

### 4.3.4 Input Pulse Width

We next verified that the deconvolution used to calculate the impulse response was sufficiently accurate. To generate the impulse response, we ideally would use a pulse train of Dirac delta functions as the input to the sampler. However, any pulsed input in SPICE has finite width. Therefore, the input pulse must be deconvolved from the output response in our impulse response simulations. We used trapezoidal pulses such as those shown in Fig. 4-7 with rise- and fall-times of 0.5 ps and with pulse width,  $t_{pw}$ .

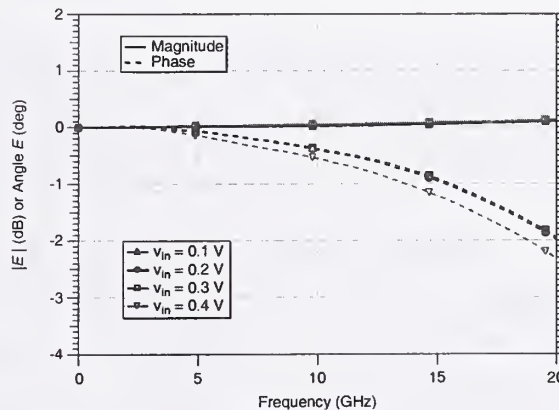


Figure 4-10. Magnitude and phase of  $E(f)$  of the nose-to-nose simulations with various input levels,  $v_{in}$ . The similarity of the correction factors indicates that a 0.2 V input signal or DC offset will be well within the small-signal regime of our sampling circuit model.

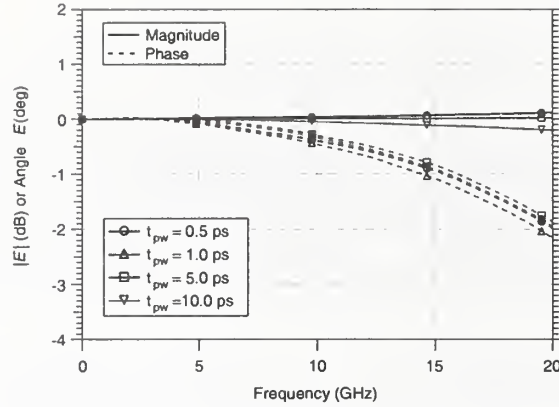


Figure 4-11.  $E(f)$  for the Riad sampler with various input pulse widths,  $t_{pw}$ . Very little variation in the phase component of  $E(f)$  is seen. We use an input pulse width of 0.5 ps in our SPICE simulations.

As shown in Fig. 4-11, there is very little difference in the phase component of  $E(f)$  when using different pulse widths, indicating that our deconvolution process is adequate. In our SPICE simulations, we used the smallest  $t_{pw}$  of 0.5 ps. For input pulse widths smaller than this, the maximum timestep in the SPICE simulation had to be decreased, reducing computational efficiency.

#### 4.4 More Details on the SPICE Simulations

Table 4-2 summarizes our default simulation settings. These settings are chosen to maximize computation efficiency while accurately resolving details in the parametric studies discussed in Section 5. Additional details on the SPICE simulations are found below. The SPICE code itself is found in Section 4.5.

##### 4.4.1 Impulse Response Calculations

In our default SPICE simulations, the impulse response was found by performing a transient simulation over a large number of sampling cycles. A typical impulse-response simulation covered 85 ns. With a sampling-cycle period of 500 ps, that was 170 cycles. We made the strobe repetition period 501 ps, and the impulse repetition period

Table 4-2. Summary of default simulation settings

Simulation Parameter	Value
Maximum time step, $t_{step}$	0.5 ps
Sampling-cycle period, $t_{smp}$	500 ps
Input voltage level, $v_{in}$	0.2 V
Input pulse width, $t_{pw}$	0.5 ps

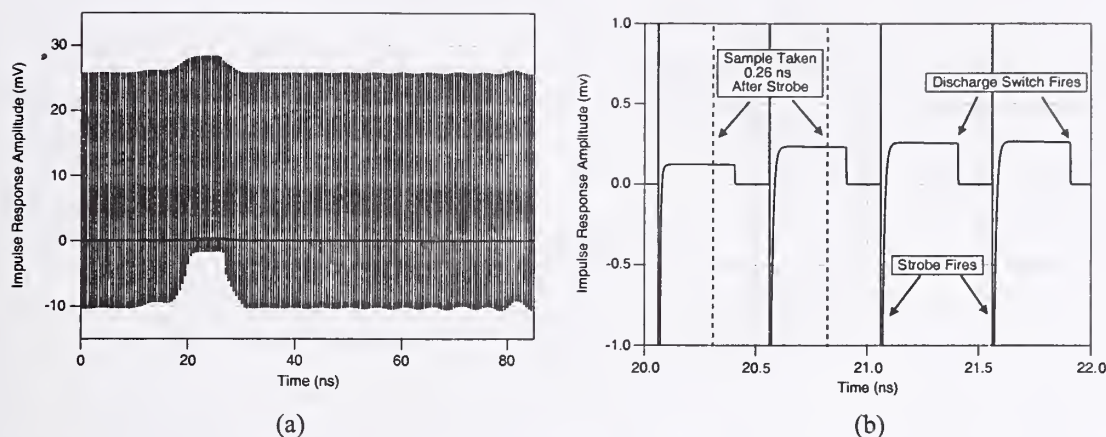


Figure 4-12. Plots of the time record directly resulting from the SPICE simulations of the impulse response. (a) The entire time record. Note the impulse response can be seen from ~10 ns to 30 ns. (b) A close-up of the same time record. The large pulses are the strobe firing, the small plateaus correspond to the charge stored on the hold capacitors in response to the input pulse train of very short pulses, and the rapid drop-offs of the plateaus correspond to the discharging of the hold capacitors by the switches.

500 ps, for a  $t_{\text{delay}}$  (see Fig. 4-7) of 1 ps. We found empirically that 1 ps offered sufficient resolution of the input pulse train for the impulse response calculation.

As mentioned previously, we inserted switches around the hold capacitors to discharge the capacitors after each sample was taken. This allowed us to use a shorter sampling period and provided greater computational efficiency than if we had to wait for the capacitors to discharge on their own, as occurs in physical samplers. The switches in our default simulations fired 365 ps after the strobe fired. This time delay was found to be sufficient to enable complete reconstruction of the impulse response. See Fig. 4-12 for plots of the time record of a typical impulse response simulation.

#### 4.4.2 Kickout Pulse Calculations

The kickout pulse was generated in a second SPICE transient simulation with a much shorter time record. We applied an offset DC voltage to the bias lines, and performed a simulation over a small number of sampling cycles. In a typical calculation, we specified a transient simulation running from 9.0 ns to 9.35 ns. The delay in starting the kickout record gave the DC voltages in the sampler a chance to settle before we started collecting data. Again, the switch fired to discharge the hold capacitors 365 ps after the strobe fired. See Fig. 4-13.

#### 4.4.3 Nose-to-Nose Calculation and Error

Once the impulse time record and kickout pulse were generated and saved to a data file (the impulse response time record is typically 5 to 10 Mb), the two files were imported into an external analysis program. This program first sampled the impulse-response time record periodically at a user-specified point in time relative to the strobe pulse. We used a sample time of 0.26 ns after the strobe fires, a bit more than halfway

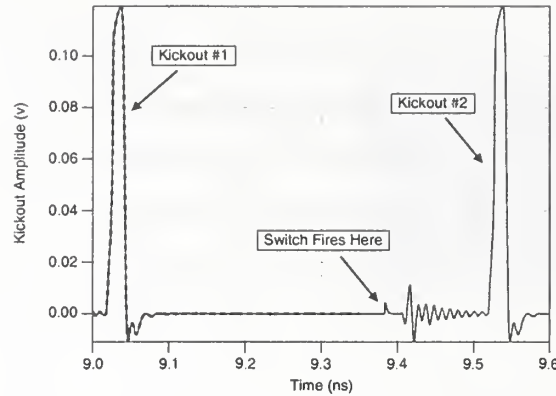


Figure 4-13. One complete cycle of the kickout pulse. The wavy line indicates that the hold capacitor discharge switches have fired. The thicker dashed line shows the length of a typical kickout pulse simulation.

between strobe pulses, as shown in Fig. 4-12(b). The program then deconvolved the input pulse from the impulse response time record to find the actual impulse response of the sampler. This operation was done in the frequency domain, where deconvolution becomes division of two frequency responses. The program then multiplied the frequency-domain representations of the kickout pulse and impulse response to form the nose-to-nose response (multiplication in the frequency domain is equivalent to convolution in the time domain). Finally, the program divided the square root of the nose-to-nose response by the impulse response to form the error term, as defined in eq (2-4). The magnitude and phase components of the error term were then saved to output files. The phase was detrended according to the process described in Section 2.4 using a second external program.



## Appendix for Section 4. SPICE Code

The actual SPICE code used in our simulations follows. To run this code, we concatenate the "Sampler.txt" file with either the "impulse.txt" or the "kickout.txt." The code runs in SPICE3.

### Sampler.txt:

```
Sampler
** A spice model for the HP-1430A sampler.
** From Sedki M. Riad, "Modeling of the HP-1430A feedthrough wide-band (28-ps)
**   sampling head," IEEE Trans. Instrumentation and Measurement, vol. IM-31,
**   no. 2, pp. 110-115, June 1982.
**
** This spice model includes transmission lines to shape the strobe pulse
** and to allow the strobe impedance to be included.
** It also includes switches to hasten the hold capacitor discharge time.
**
** To run:
** The program runs on SPICE3.
** You need to concatenate this Sampler.txt file with either Impulse.txt or Kickout.txt.
** For example, to generate the kickout pulse, on a Unix machine, type
** rm Spice.txt
** cat Sampler.txt kickout.txt > Spice.txt
** spice3 Spice.txt
** run
** set nopage
** print v(1) > kick7.dat
** quit
**
** More examples can be found in the file spice.commands.txt
**
.OPTIONS NOPAGE
** This is the sampler circuit.
** The format is: SAMPLER [input] [strobe] [output] [kickoutbias] [dischargeswitch] [ground]
**
.SUBCKT SAMPLER 23 25 30 33 70 0
**
** This is the termination impedance of the sampler.
Rterm 23 0 50
**
** The sampling diodes. For the asymmetric case, increase the area of one diode,
** decrease the other, and run two SPICE simulations with + and - offset voltages
** for the kickout pulse. Only one impulse response simulation.
D1 23 24 DIODE_SAMPLE9 1.0
** Second diode is connected between 26 and 23
D2 26 23 DIODE_SAMPLE9 1.0
**
** The diode bias supply
** The hold capacitors discharge through these diode bias resistors.
** Adjusting them changes the hold time.
** These resistors also change the tail of the sampler impulse response.
** Smaller values of resistor reduce the tail.
rbias1 24 31 3600
vbias1 31 33 1.63
rbias2 26 32 3600
vbias2 32 33 -1.63
**
** Voltage controlled switches discharge the hold capacitors.
** They use the model SWMODEL.
** The last two parameters are the controlling voltage nodes.
S3 24 31 70 0 SWMODEL OFF
S4 26 32 70 0 SWMODEL OFF
**
```

```

**
** The hold capacitors. These values are not defined in Riad's paper.
Chold1 24 10 4pF
Chold2 26 11 4pF
**
** The source impedance of the strobe. Riad thinks this is 57 ohms total.
** So each should be 57/2 ohms = 28.5 ohms.
Rsource1 25 10 28.5
Rsource2 27 11 28.5
*Rsource1 25 10 50
*Rsource2 27 11 50
**
** A distributed LC model for the transmission lines that shape the strobe voltage.
** Riad says that these have Z0=85.2 ohms and Td=22.2ps.
** To maintain consistency with previous calculations, we will use Td=7ps.
** The inductance per unit length: L=Z0/c (c=3E8 m/s=speed of light)
** The capacitance per unit length: C=1/(Z0*c)
** The total length: l=TD*c (Model values: L'=l*L/6, C'=l*C/2)
Ltrans1 10 42 0.1nH
Ltrans2 11 43 0.1nH
Ctrans1 42 43 0.041pF
Ltrans3 42 44 0.1nH
Ltrans4 43 45 0.1nH
Ctrans2 44 45 0.041pF
Ltrans5 44 46 0.1nH
Ltrans6 45 47 0.1nH
** These switches terminate the transmission line with its characteristic impedance
** during the hold capacitor discharge cycle.
Strans1 46 0 70 0 SWMODELTR OFF
Strans2 47 0 70 0 SWMODELTR OFF
** These switches discharge the hold capacitors and keep the transmission lines
** from ringing when the strobe turns off.
S5 10 0 70 0 SWMODEL OFF
S6 11 0 70 0 SWMODEL OFF
**
** The voltage strobe is connected to 25.
** This is the inverted strobe.
EX2 27 0 0 25 1.0
**
** These amplifiers sample and add the voltage injected into the capacitors.
E1 29 33 24 0 0.5
E2 30 29 26 0 0.5
**
.ENDS SAMPLER
**
** Below is half of the strobe circuit. It is set to sample every ps.
** The sampling period is 0.5 ns.
** Setting the voltage to 6V here gives a total strobe voltage of 12V.
** The strobe turns on, then stays on until we discharge the hold capacitors.
** Then the strobe turns off.
** Format is PULSE([V start] [V pulse] [time delay] [rise time] [fall time] [pulse width] [period])
.SUBCKT STROBE 40 41
vstrobe 40 41 DC 0 PULSE(0 6 0NS 10PS 1PS 356PS 0.501NS)
.ENDS STROBE
**
** These are the diode parameters.
** Diode model for a Schottky barrier diode. RS is and Cj can be up in the sampler
.model DIODE_SAMPLE9 D (IS=2.67e-11 N=1.08 VJ=0.7 M=0.5 EG=0.69 CJO=0.045pF RS=19)
** These are the switch parameters.
.model SWMODEL SW (VT=1 VH=0 RON=0.1 ROFF=100000)
.model SWMODELTR SW (VT=1 VH=0 RON=42.6 ROFF=0.1)
.model SWMODEL1 SW (VT=1 VH=0 RON=100000 ROFF=.01)
.model SWMODEL2 SW (VT=1 VH=0 RON=.01 ROFF=100000)
**

```

## impulse.txt

```
**
*****
** Type "print v(4) > time.txt" to save the impulse response. *
*****
**
** Put in a delay in the input impulse so that it starts well after the first sampling pulse ends.
** This is needed because the sampler responds to signals at its input during the duration of the
** sampling pulse and even slightly after the sampling pulse has ended.
** This offset is t_0(=0.06ns in this case).
** Do not make vin too large, as a large vin will turn the diodes on.
** Format is PULSE([V start] [V pulse] [time delay] [rise time] [fall time] [pulse width] [period])
vin 1 0 DC 0 PULSE(0 0.2 0.06NS 0.5PS 0.5PS 0.5PS 0.5NS)
rin 1 2 50
** This is the control for the discharge switches for the hold capacitors.
** Format is PULSE([V start] [V pulse] [time delay] [rise time] [fall time] [pulse width] [period])
vswitch 6 0 DC 0 PULSE(0 5 365PS 1PS 1PS 20PS 0.501NS)
** One half of the strobe source
XS1 0 3 STROBE
** Sampler format is: SAMPLER [input] [strobe] [output] [kickoutbias] [dischargeswitch] [ground]
X1 2 3 4 0 6 0 SAMPLER
** The simulation: Format is .tran [tstep] [tstop] [tstart] [tmax]
** tstep = tmax = max time step (make smaller to smooth out plots)
.tran 0.0005ns 85ns 0 0.0005ns
.end
```

## kickout.txt

```
**
*****
** For symmetric diodes case: type "print v(1) > kick.txt" to save the kickout waveform. *
** For asymmetric case: type "print v(1) > kick.txt" to save the first kickout waveform. *
** Then change the voltage in vcap to -0.2, rerun, and type "print v(1) > kick1.txt" to *
** save the second kickout waveform. *
*****
** Check the kickout pulses to see when they settle down. Then
** choose a suitable delay. This same delay should probably used for the other signals too.
**
** The time delay of the switch should be greater than the point where
** the actual voltage sample is taken (externally)
vcap 5 0 0.2
** One half of the strobe source
XS1 0 3 STROBE
** Format is PULSE([V start] [V pulse] [time delay] [rise time] [fall time] [pulse width] [period])
vswitch 6 0 DC 0 PULSE(0 5 0.365NS 1PS 1PS 20PS 0.501NS)
rin 1 0 50
** Sampler format is: SAMPLER [input] [strobe] [output] [kickoutbias] [dischargeswitch] [ground]
X1 1 3 4 5 6 0 SAMPLER
** The simulation: Format is .tran [tstep] [tstop] [tstart] [tmax]
.tran 0.0005ns 9.35ns 9ns 0.0005ns
**
```

## spice.commands.txt

This file gives the actual commands to generate the kickout pulse or impulse response in SPICE. One can copy and paste these commands directly onto the command line of a computer capable of running SPICE3.

```
** Impulse response simulations
rm Spice.txt
cat Sampler.txt impulse.txt > Spice.txt
spice3 Spice.txt
run
set nopage
print v(4) > time7.dat
exit
```

```
vi time7.dat
4d
:wq
```

```
** Kickout pulse simulations
rm Spice.txt
cat Sampler.txt kickout.txt > Spice.txt
spice3 Spice.txt
run
set nopage
print v(1) > kick7.dat
quit
```

```
vi kick7.dat
4d
:wq
```



## 5. Parametric Studies Using SPICE

In this section, we investigate the sensitivity of the nose-to-nose calibration to variation in sampling-circuit component values. We systematically varied individual circuit element values in our default sampling-circuit model and noted changes in the magnitude and phase of the correction factor,  $E(f)$ . These sets of simulations clearly demonstrate which sampling-circuit elements dominate the phase error in the nose-to-nose calibration and how sensitive the phase error is to variation in component values.

As mentioned in Section 1, this type of study would be practically impossible to conduct experimentally due to fabrication and measurement limitations. In addition, we do not know the specifics of the actual sampling-circuit component values. However, based on the sampling circuits described in Refs. [19] and [24], we can estimate a realistic *range* of values for this particular sampling-circuit configuration. Using the parametric studies presented in this section as a foundation, in Section 6 we quantify the sensitivity of the phase error by generating a combined uncertainty statement for a given range of parameter values.

The parametric studies below used the default sampler model developed in Section 4.2 (a model based on Ref. [19], with no packaging parasitics and faster strobe-excitation-pulse rise time). For each model parameter, we describe the role it plays in the sampling circuit, the range of parameter values that we chose, and show graphical simulation results of the corresponding correction factor,  $E(f)$ .  $E(f)$  (defined in Section 2.4) describes how different our nose-to-nose-derived estimate of the sampler's impulse response is from the true impulse response for a given model. The dashed curve in each plot represents the error in the phase component of the impulse-response estimate when compared to the impulse response derived using the method described in Section 2.2.

Because the nose-to-nose calibration is theoretically exact for ideal samplers (see Section 3.2 and Refs. [3, 4, 15, 20]), we find that the errors in the calibration depend on the nonidealities of real sampling circuits, such as using a shorted transmission line to shape the strobe pulse, and using diodes with nonlinear junction capacitance as switches. We will see that the diode's nonlinear junction capacitance and its interaction with other circuit elements is especially important. As will be shown, some of these interactions are quite complicated. While we provide analytic descriptions for some of these interactions, we must rely on the numerical techniques for the bulk of the analysis.

### 5.1 Sampling Diode Model Parameters

#### 5.1.1 Description

Schottky-barrier diodes are used in the samplers we studied, and their operation can be modeled quite accurately with a few important parameters [21]. Equations relating these parameters to the diode's large-signal behavior are used in SPICE [22], as discussed in detail in Section 3.1. We repeat relevant equations here for convenience. Specifically, the large-signal current through the diode is given by

$$I(V_j) = I_s \left( \exp\left(\frac{qV_j}{nkT}\right) - 1 \right), \quad (5-1)$$

where  $V_j$  is the large-signal voltage across the diode junction (not including the drop across the spreading resistance  $R_s$ ),  $I_s$  is the reverse saturation current,  $q$  is the charge on an electron,  $n$  is the ideality factor,  $k$  is the Boltzmann constant, and  $T$  is the temperature (K). The diode junction capacitance is:

$$C_j(V_j) = \frac{C_{j0}}{\left(1 - \frac{V_j(t)}{\phi_{bi}}\right)^\gamma}, \quad (5-2)$$

where  $C_{j0}$  is the zero-voltage junction capacitance (note that  $C_j = C_{j0}$ , a constant, when  $V_j = 0$ ),  $\phi_{bi}$  is the junction's built-in potential, and  $\gamma$  is the grading coefficient ( $\gamma = 0.5$  for Schottky-barrier diodes [21]).

We divide our parametric studies of the diode model parameters into two categories: those involving all diode parameters except junction capacitance and those involving  $C(V_j)$ . We do this because variation of most diode parameters has little effect on the phase error in the nose-to-nose estimation of the impulse response, while the nonlinearity associated with the diode's junction capacitance has a significant effect. We include the built-in potential,  $\phi_{bi}$ , of the diode junction in the first category since it is shown to have little effect on the phase error. We also include a section with results for Kerley's split diode model discussed in Section 4.1.2 and shown in Fig. 4-2(c).

Diode parameters for our default sampler model (Table 4-1) are reproduced below in Table 5-1 for convenience. Parametric studies were conducted to cover the range of both the Riad (default) and the Kerley models, and to go somewhat outside this range.

## 5.1.2 Simulation Results

### 5.1.2.1 Diode Model Parameters Except Junction Capacitance

Figures 5-1(a) through (d) show changes in the phase component of  $E(f)$  as we varied diode parameters other than those related to junction capacitance. We see that

Table 5-1. Diode model parameters.

	$R_s (\Omega)$	$I_s$ (pA)	$n$	$C_{j0}$ (fF)	$\phi_{bi}$ (V)	$\gamma$	$E_G$ (eV)	$\tau_t$ (ps)
Riad model	19	26.7	1.08	45	0.7	0.5	0.69	0
Kerley model	10	0.03	1.0	40	1.0	0.5	1.11	0
Default model	19	26.7	1.08	45	0.7	0.5	0.69	0

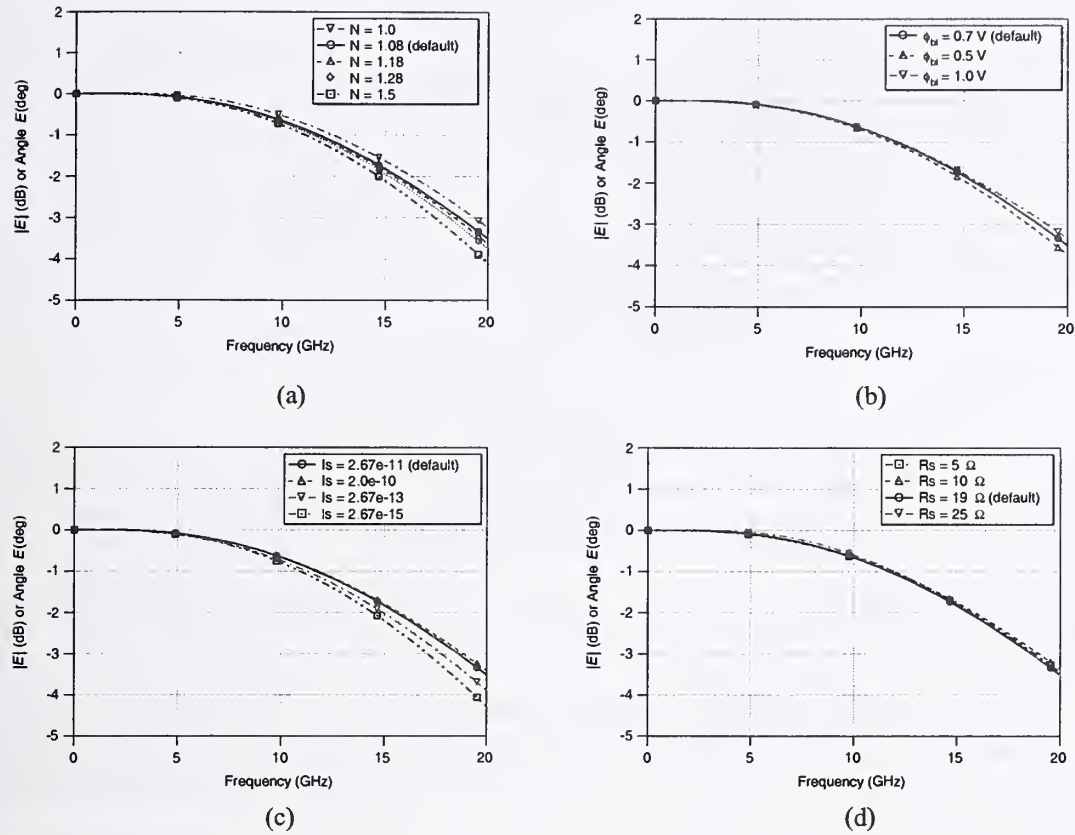


Figure 5-1. Phase of the correction factor,  $E(f)$ , of nose-to-nose simulations as we vary diode parameters: (a) Ideality factor,  $n$ ; (b) Built-in potential,  $\phi_{bi}$ ; (c) Saturation current,  $I_s$ ; (d) Spreading resistance,  $R_s$ . The maximum change in the phase component of  $E(f)$  is approximately  $1^\circ$  for this set of parametric studies.

these diode parameters change the phase error of the nose-to-nose estimation by a maximum of approximately  $1^\circ$ . We found that varying the energy gap,  $E_G$ , has negligible effect on the phase error, so do not include it here. As mentioned in Section 3.1, SPICE uses  $E_G$  to differentiate between different types of diodes.

### 5.1.2.2 Parameters Involving Diode Junction Capacitance

Figure 5-2 shows that the correction factor,  $E(f)$ , increases as the zero-voltage junction capacitance,  $C_{j0}$ , increases. As shown in eq (5-2), increasing  $C_{j0}$  results in stronger nonlinearity of the diode junction capacitance,  $C(V_j)$ . The corresponding increase in the phase error is explained in Section 3.2 and Refs. [15, 20]. Note that the variation in  $C_{j0}$  in this example is more extreme than we may expect in a real Schottky-barrier diode. Component variation is typically no more than  $\pm 25\%$  ( $\sim 0.034$  pF to  $\sim 0.056$  pF), and is generally closer to  $\pm 10\%$ , according to the data sheet for a GaAs Schottky-barrier diode with a SPICE model similar to our default model [25].

Figure 5-3 shows the effect on the correction factor,  $E(f)$ , for parametric variation of the diode's grading coefficient,  $\gamma$ . We see that  $E(f)$  is positively correlated to the value of  $\gamma$ . According to eq (5-2), the larger the grading coefficient, the higher the degree of



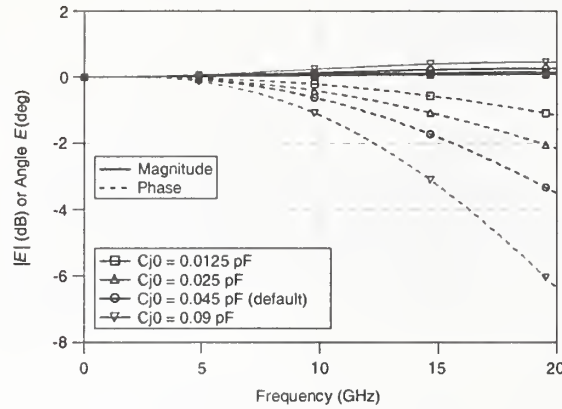


Figure 5-2.  $E(f)$  for different values of zero-voltage diode junction capacitance.  $C_{j0} = 0.045$  pF in Riad's model,  $C_{j0} = 0.040$  pF in John Kerley's model, and  $C_{j0} = 0.025$  pF in the split-diode model in Section 4.1.2. Other model parameter values are for the default diode model specified in Table 5-1. Note that the maximum variation in  $C_{j0}$  is closer to 25 % for a Schottky-barrier diode similar to our default model [25].

nonlinearity in the diode junction capacitance.  $\gamma = 0.5$  corresponds to the default sampler model.

This simulation highlights an important conclusion that the error in the nose-to-nose calibration (magnitude and phase) is essentially zero when the junction capacitance is constant and equal to  $C_{j0}$  (for  $\gamma = 0$ ). However, constant junction capacitance is physically impossible for real diodes.

### 5.1.2.3 Split Diode Model

In Kerley's sampler model [24], three diode configurations were discussed—one with constant junction capacitance, one with the standard SPICE nonlinear junction capacitance, and one with a split-diode capacitance model, as shown in Fig. 4-2. Based on the above discussion of diode junction capacitance, we expect that the constant-junction-capacitance model will have zero phase error and that the split diode model will have a phase error somewhat lower than that of the default diode model. These results are shown in Fig. 5-4.

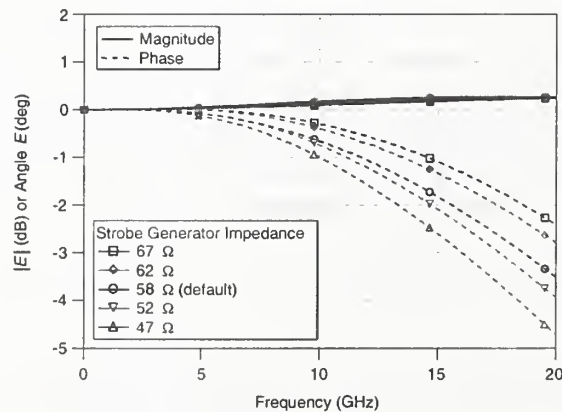


Figure 5-3.  $E(f)$  for various values of grading coefficient,  $\gamma$ . Note that the error in the nose-to-nose calibration is nearly zero when the junction capacitance is constant (for  $\gamma = 0.0$ , a physical impossibility).



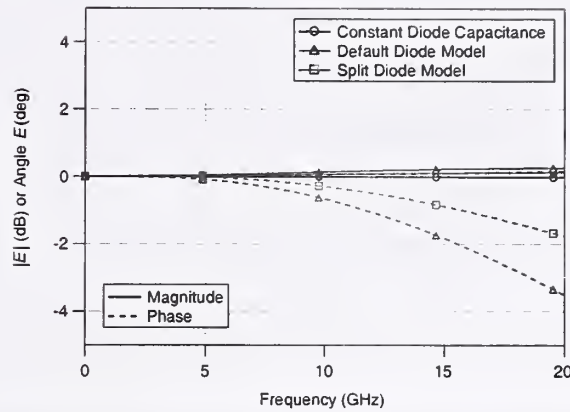


Figure 5-4.  $E(f)$  for the three diode models shown in Fig. 4-2.

The default sampler model has the most conservative (highest) estimate of  $E(f)$ . The diode manufacturer has stated that the split model is probably the most accurate [24], so we expect that the error in real nose-to-nose calibrations due to the sampling circuitry will be somewhat smaller than that predicted using our default model.

## 5.2 Hold Capacitors

### 5.2.1 Description

The hold capacitors collect and store charge in an amount that is ideally proportional to the input signal during each sampling cycle, as discussed in Section 2.1. Charge is also transferred to the hold capacitors by the strobe pulse each sampling cycle, although the voltages induced by this charge ideally cancel at the output amplifier (since they are of opposite polarity). Here we investigate how charging the hold capacitors during each sampling cycle affects the nose-to-nose calibration by changing the impedance presented to the sampling diodes.

As discussed in Refs. [2] and [15], the RC time constant associated with the strobe generator impedance and hold capacitor is generally much longer than the aperture time of the sampling circuit. Hence, the hold capacitor appears almost as a short to the diode circuit during the aperture time. For example, in our default sampler model, the RC time constant of one branch of the  $57\ \Omega$  strobe generator and the  $4\ \text{pF}$  hold capacitor is  $(28.5) \times (4 \times 10^{-12}) = 114\ \text{ps}$ , while the aperture time is approximately  $10\ \text{ps}$  [2]. Therefore, in the default sampler model, we expect to see little effect on the circuit's impedance due to charging of the hold capacitor.

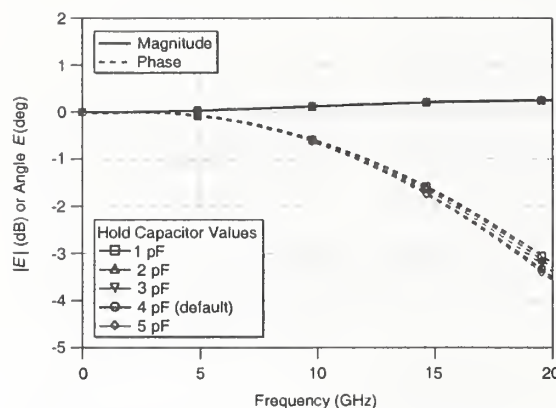


Figure 5-5.  $E(f)$  as a function of hold capacitor value.

The hold capacitor value in Kerley's model of the sampler is given as 2 pF, the value also given by Verspecht and Rush in Ref. [2]. We conducted simulations with hold capacitor values ranging from 1 pF to 5 pF, with 4 pF our default model value.

## 5.2.2 Simulation Results

As expected, in Fig. 5-5 we see little effect on the phase error for the various  $C_H$  values, with the overall increase in phase error less than half a degree at 20 GHz for the smallest value of hold capacitor, 1 pF.

## 5.3 Strobe-Generator and Strobe Pulse-Shaping Circuitry

In our parametric studies, the strobe-pulse circuitry is seen to have a significant effect on the phase error in the nose-to-nose calibration. Many of these effects can be linked to interaction of the strobe and the sampling diode's nonlinear junction capacitance. As discussed in Section 3.2, the phase error introduced into the nose-to-nose calibration by the nonlinear junction capacitance arises from the requirement for charge conservation as the diodes turn on and off. The strobe pulse will naturally have an impact on this transition.

As a result, the way that we model the strobe pulse, including its rise time, amplitude, and the strobe-generator impedance, will affect the operation of the sampling diodes, and thus affect  $E(f)$ . That is, in the physical sampler, the strobe pulse and input pulses utilize separate ground schemes, so the direct effect of the strobe generator impedance on the small-signal behavior of the sampler is difficult to accurately model. In the following subsections we look at the effect of these strobe pulse-related parameters on the estimated error in the nose-to-nose calibration.

### 5.3.1 Ideal Source and Transmission Line Pulse Shaping

#### 5.3.1.1 Description

In the original nose-to-nose analyses [2-4] and in our earlier work [16], the strobe generator was modeled as an ideal voltage source with source impedance of  $0 \Omega$ . In Ref.

[16], this ideal strobe pulse is trapezoidal, with rise- and fall-times and pulse width specified as SPICE parameters. However, the sampling circuits described in Riad [19] and in Kerley [24] characterize the strobe using a step generator with a given source impedance that drives a shorted transmission line. Reflection of the leading edge of this step pulse off the shorted end of the transmission line turns the strobe pulse off.

To implement this transmission-line-based strobe generator in our default sampling-circuit model, we used a strobe excitation pulse consisting of a long-duration ideal trapezoidal pulse, effectively a step pulse. This step pulse excites a shorted transmission line which we modeled with lumped elements. In our model and in Ref. [19], the transmission line has a characteristic impedance  $Z_0$  of 85.2  $\Omega$ .

The strobe is applied differentially across the two sampling-circuit branches with the input port at zero potential, as shown in Fig. 4-1. To model this, we applied two strobe excitation pulses, one positive and one negative, across the two sampler branches. The strobe excitation pulse generator had a 57  $\Omega$  source impedance ( $R_{\text{strobe}} = 28.5 \Omega$  in Fig. 4-1), and the strobe excitation amplitude was 12 V (Strobe Excitation and Inverted Strobe Excitation equal  $\pm 6$  V respectively in Fig. 4-1). Below we examine the effects on the error in the nose-to-nose calibration of using the realistic, transmission-line-shaped strobe pulse rather than the perfect trapezoidal pulse of Ref. [16].

We performed simulations using the two types of strobe pulses. We used two different strobe-pulse rise times to see whether the effect of rise time on the phase error was similar for both types of sources. The transmission line strobe source was excited with step pulses having both 10 and 15 ps rise times (our default sampling-circuit model has an excitation-pulse rise time of 10 ps). The ideal-source strobe pulses had 15 and 20 ps rise times. We chose these rise time values to give approximately the same  $dV/dt$  for the two types of sources. Theoretically the pulse width is not critical as long as the sampling diodes are forward biased long enough to induce a charge proportional to the input signal on the hold capacitors.

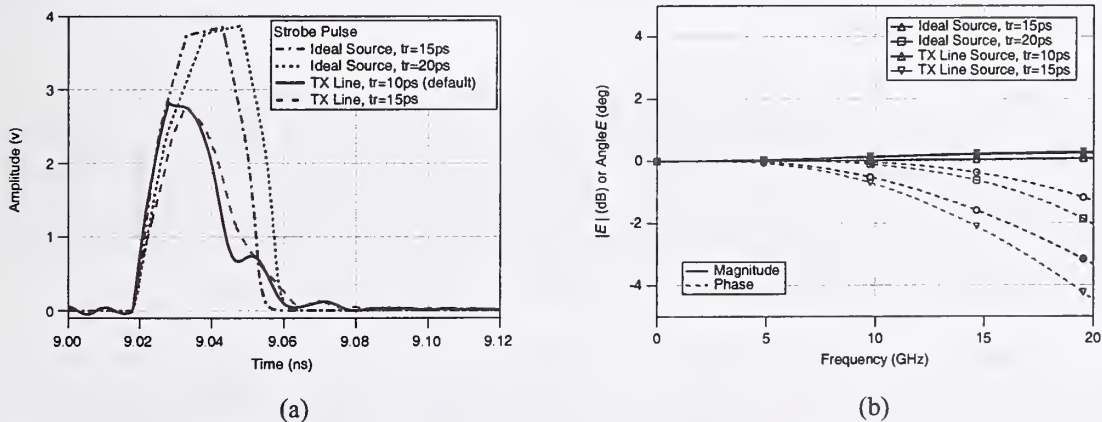


Figure 5-6. Comparison of strobe pulses formed using ideal pulse sources and realistic, transmission-line pulse shaping. (a) Strobe pulses in the time domain; (b)  $E(f)$  associated with these strobe pulses.



### 5.3.1.2 Simulation Results

Figure 5-6(a) compares strobe pulses formed using the SPICE ideal pulse source to those using the shorted transmission line described above. The correction factor,  $E(f)$ , associated with these different strobe sources is shown in Fig. 5-6(b). We see an increased phase error with the transmission-line-shaped strobe. This increase in error can be attributed, at least in part, to the interaction of the reactances of the realistic strobe source (the transmission line is a ladder network consisting of inductors and capacitors) with the diode's nonlinear junction capacitance, rather than the difference in shape between the two types of strobes. The key to this argument is shown in Fig. 5-4, where we see essentially zero magnitude and phase error for a constant diode junction capacitance, even when the transmission line based strobe circuitry is used.

### 5.3.2 Strobe-Pulse Rise Time

#### 5.3.2.1 Description

In this subsection, we demonstrate that the strobe-pulse rise time has a significant effect on the phase error in our simulations of the nose-to-nose calibration. When the strobe has a longer rise time, the diode junction capacitance must maintain charge conservation for a longer time before the diode conducts, as discussed in Section 3.2. This causes the small-signal junction voltage to change instantaneously, inducing a corresponding change in the kickout pulse before and after the diode conducts.

The 10 ps rise time of the default model value was chosen to approximate the 50 GHz input bandwidth of the sampling heads used in nose-to-nose measurements, as opposed to the longer rise times in the Riad (32 ps) and Kerley models. These models were based on sampling circuits with 20 GHz input bandwidths. In the following, we chose strobe-excitation-pulse rise time values ranging from 5 to 20 ps. The excitation pulse incident on the transmission line described creates the strobe pulse.

#### 5.3.2.2 Simulation Results

Figure 5-7(a) shows the strobe pulse for various strobe-excitation-pulse rise time ( $t_r$ ) values. This figure is reproduced from Section 4.2.2 [Fig. 4-6(a)], where we described how we chose the strobe pulse rise time for our default model. Note that the default sampling-circuit model has a strobe excitation-pulse rise time of 10 ps, while the rise time of the strobe pulse itself will be somewhat different from excitation-pulse rise time due to interaction of the transmission line impedances with other circuitry.

An increase in the phase error with longer strobe-pulse rise time is shown in Fig. 5-7(b). To explain this increase in error, we turn to the time domain. Figure 5-8 shows a plot of kickout pulses and impulse responses with different strobe-excitation-pulse rise times. Two things are noteworthy in Fig. 5-8: first, the full-width, half-maximum (FWHM) width of the kickout pulse or impulse response is narrower with a longer strobe



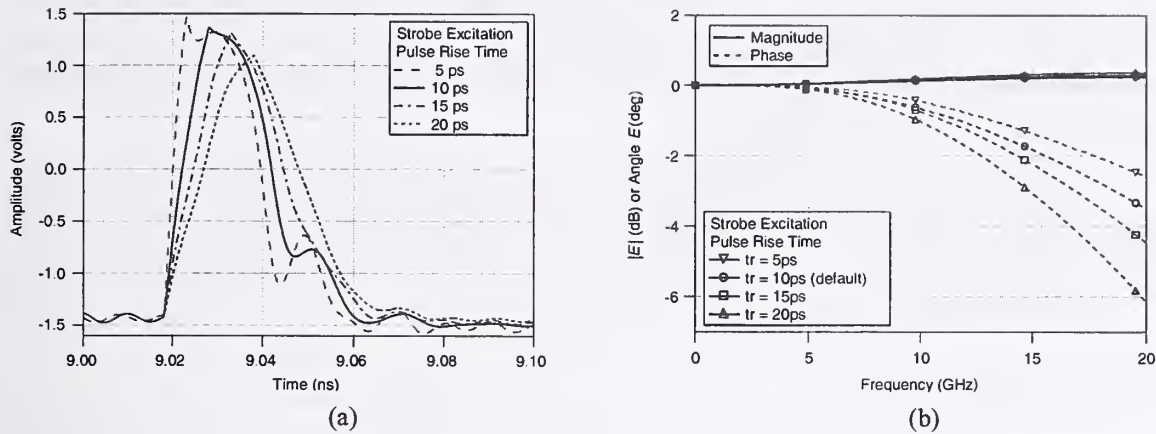


Figure 5-7. (a) Strobe pulses and (b)  $E(f)$  for different strobe-excitation-pulse rise times.

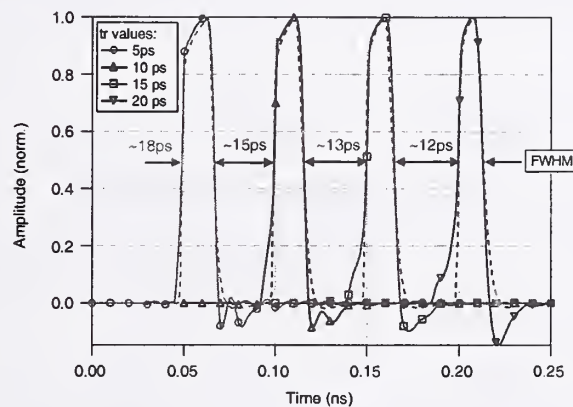


Figure 5-8. Kickout pulses (solid lines with symbols) and impulse responses (dashed lines) for several different strobe-pulse rise times. Note that the kickout becomes less similar to the impulse response for longer rise times. The time axis has been shifted to better illustrate the differences.

pulse rise time. This is because the diode's aperture time is shorter when the strobe pulse rise time is longer [see Fig. 4-6(b)] for the sampling-circuit configuration we use.

The second item of interest is that, as the strobe-excitation-pulse rise time increases, the effect of the nonlinear capacitance on the kickout pulse becomes more pronounced. This effect, caused by charge conservation, as discussed in Section 3.2, is to broaden the rising edge and to introduce more undershoot on the falling edge of the kickout pulse with respect to the impulse response of the sampler.

### 5.3.3 Strobe-Generator Impedance

#### 5.3.3.1 Description

The impedance of the strobe generator is modeled as a resistance in series with the strobe source, called  $R_{\text{strobe}}$  in Fig. 4-1. As mentioned above, our SPICE model uses two sources to represent the strobe generator. We use a value for  $R_{\text{strobe}}$  equal to half the

total generator impedance in each branch. In the physical sampler, the strobe pulse and input pulses utilize separate ground schemes. The model presented here is an approximation based on the characteristic impedances of waveguiding elements associated with the strobe source.

The default value of strobe-generator impedance is  $57\ \Omega$ , which is distributed across the two sampling-circuit branches as lumped resistors of  $28.5\ \Omega$  each. We chose strobe generator impedances ranging from  $47\ \Omega$  to  $67\ \Omega$ , corresponding to values of  $R_{\text{strobe}}$  ranging from  $23.5\ \Omega$  to  $33.5\ \Omega$ .

### 5.3.3.2 Simulation Results

Figure 5-9 shows that the strobe-generator impedance can have a significant effect on the phase component of the phase error. The reason why the phase error increases for smaller values of  $R_{\text{strobe}}$  is not so obvious, especially when we look at the time domain representation of the kickout pulse (solid lines) and impulse response

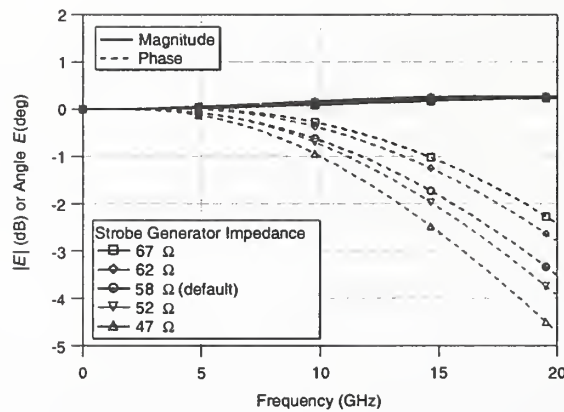


Figure 5-9. Effect of changing the strobe-generator impedance on  $E(f)$ .

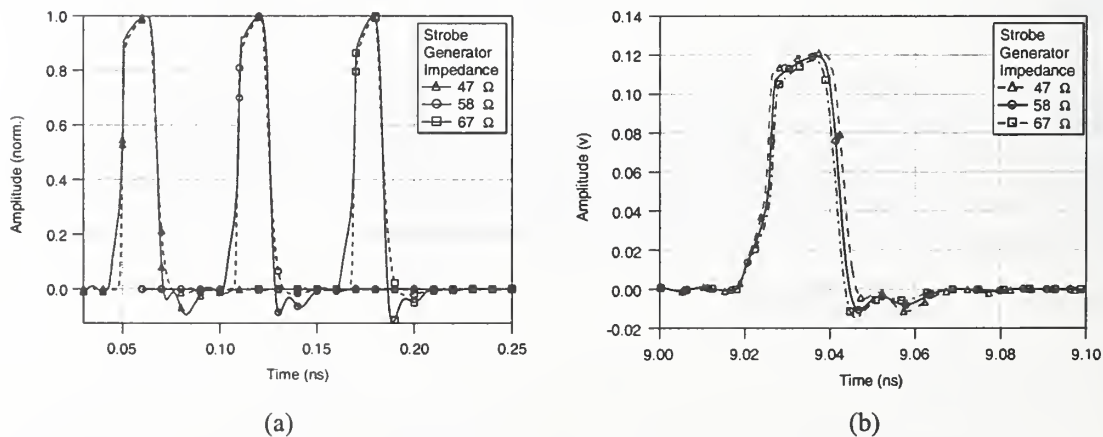


Figure 5-10. Kickout pulses (solid) and impulse responses (dashed) for different values of strobe-generator impedance. (a) Time axis shifted for better resolution; (b) Non-time-shifted, non-normalized kickout pulses.

(dashed lines) in Fig. 5-10(a). The shapes of the impulse response and kickout pulse look similar for all strobe-generator impedance values in this figure. The time axis has been shifted in Fig. 5-10(a) for better resolution of the kickout pulse and impulse responses.

Figure 5-10(b) is the non-time-shifted, non-normalized representation of the kickout pulses. Here we see that, for smaller values of  $R_{\text{strobe}}$ , the undershoot in the kickout pulse occurs later in time relative to the main lobe. The effect on the phase error of small error pulses such as the undershoot pulse is magnified when those pulses occur delayed in time relative to the main pulse. This effect is discussed in detail in the appendix of this section, where we demonstrate that a phase-error term proportional to the *cube* of the delay ( $t_1$  in the appendix) will be generated for error pulses that are similar to the undershoot pulses shown in Fig. 5-10. Thus, even a small pulse will have a significant effect on the phase error when the delay is long.

### 5.3.4 Strobe-Excitation Pulse Amplitude

#### 5.3.4.1 Description

As discussed above, the strobe pulse in our SPICE model is implemented by the reflection of an excitation step pulse off of a shorted transmission line. In our model implementation, the excitation-pulse generator consists of two sources. One generates a positive-going step pulse applied to the anode of one sampling diode, and the other generates a negative-going step pulse applied to the cathode of the other diode, as shown in Fig. 4-1. The amplitude of each source is half of the total specified strobe voltage.

The total strobe-pulse amplitude specified in the Riad sampler model was 12 V, and the strobe pulse amplitude in the Kerley sampler model was somewhat lower. Therefore, we chose a range of values from 8 V to 16 V for this parametric study.

#### 5.3.4.2 Simulation Results

Figure 5-11 shows the effect on the correction factor  $E(f)$  when we changed the strobe excitation pulse amplitude in our nose-to-nose simulations. We see that when the

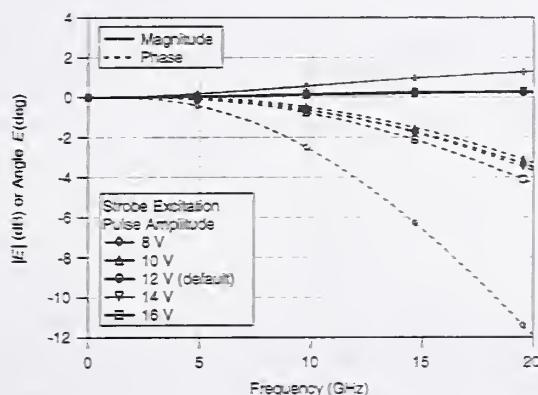


Figure 5-11.  $E(f)$  calculated for various values of strobe excitation pulse amplitude.



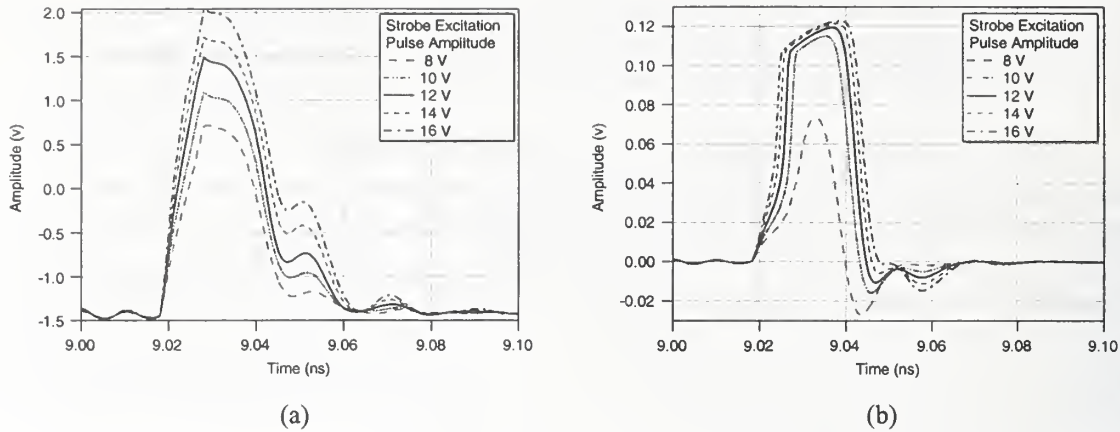


Figure 5-12. Variations in strobe-excitation-pulse amplitude. (a) Strobe pulses; (b) Kickout pulses.

strobe is large enough to turn on the diodes strongly (10 V to 16 V), the phase error changes by at most  $1^\circ$  from the default model value. The 8 V case does not turn the sampling diodes on sufficiently (seen by the large increase in both magnitude and phase of  $E(f)$ ) and is not included in the uncertainty calculation of Section 6.

Figure 5-11 shows that the relative spread in phase error is not as great as it was for variation in the strobe-excitation pulse rise time, shown in Fig. 5-7(b). The reason becomes evident when we compare strobe pulses as they appear across the sampling diodes for various amplitudes of the strobe-excitation-pulse in Fig. 5-12(a). We see that  $dv/dt$  (corresponding to the strobe rise time) is more similar at the diode forward-bias voltage of  $\sim 0.6$  V for both large and small excitation-pulse amplitudes than it is when we vary the strobe rise time, shown in Fig. 5-7(a). These graphs use the same time axis scale.

Because  $dv/dt$  is greater for larger amplitude strobes, as shown in Fig. 5-12(a), we might expect that the phase error would be smaller for these cases. We saw this was the case when we varied strobe-excitation-pulse rise times in Section 5.3.2 above. However, neglecting the 8 V case, Fig. 5-11 shows that the phase component of the error is, in fact, slightly *larger* for faster strobe-pulse rise times. We see why this is the case when we look at Fig. 5-12(b). Here we see that the undershoot on the kickout pulse occurs latest in time and with the largest amplitude for the 16 V strobe-excitation pulse. As discussed in Section 5.3.3 above, the greater the time delay corresponding to an error pulse (for example, the undershoot pulse), the greater the phase error. See the appendix to this section for more information.

## 5.4 Diode Imbalance

### 5.4.1 Description

The two-diode sampler of Fig. 4-1 is designed so that the common-mode positive- and negative-going components of the strobe pulse cancel at the sampler input port and at the output amplifier. However, if the two diodes—or any other pairs of components in the sampler's two branches—are not perfectly matched, the strobe will leave a residual



charge imbalance on the hold capacitors. This results in an offset due to the strobe pulse at the input port and at the output amplifier and affects the kickout pulse generation process.

In practice, no two components can be perfectly matched, so one performs two nose-to-nose measurements, one with a positive bias offset ( $V_0$  in Fig. 4-1) and one with a negative bias offset, in an attempt to eliminate this residual common-mode signal [3-5, 12]. The kickout pulses resulting from the positive and negative offsets are averaged as

$$k(t) = \frac{k(t)_{\text{pos}} - k(t)_{\text{neg}}}{2}, \quad (5-3)$$

where  $k(t)_{\text{pos}}$  is the kickout pulse arising from a positive offset voltage and  $k(t)_{\text{neg}}$  arises from a negative voltage offset.

Diode imbalance was implemented in our parametric studies by changing the area parameter of the SPICE diode model. Values of 2 to 10 % were chosen to correspond to specifications for GaAs diodes with similar SPICE models [25], where 12.5 % variation in  $C_{j0}$  is given as typical. A 12.5 % variation in  $C_{j0}$  corresponds to a diode area imbalance of 12.5 % because area and capacitance are directly proportional by  $C = \epsilon A/d$ , where  $A$  is the area of the diode depletion region,  $d$  is its thickness, and  $\epsilon$  is the dielectric constant of the depletion region material. The area parameter in SPICE also changes the saturation current (with area) and the spreading resistance (as  $1/\text{area}$ ).

#### 5.4.2 Simulation Results

Figure 5-13 shows simulation results where we increase the area parameter for one diode junction by one-half of the nominal change in area, while decreasing the area parameter of the other by the same amount. We see that the process of averaging the kickout pulses generated by negative and positive offset voltages results in very little change in the phase error of the nose-to-nose calibration due to sampler circuitry. Because the effect of diode imbalance is negligible, it is not considered in the uncertainty calculations of Section 6.

Figure 5-14(a) shows the effect of imbalanced diodes on kickout pulse generation. We see that with increasing diode imbalance, the negative- and positive-offset-generated pulses show more discrepancy between each other. However, in Fig. 5-14(b), we see that the averaging process given in eq (5-3) results in kickout pulses that are very similar to the symmetric case.

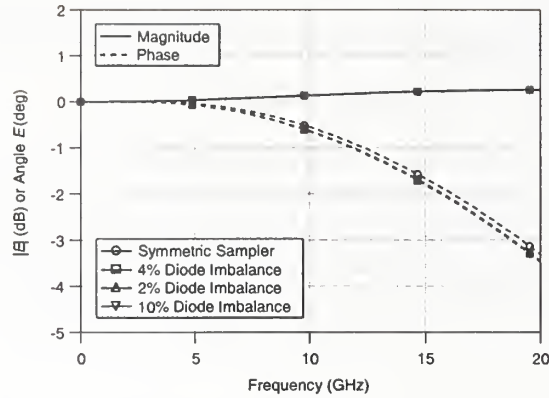


Figure 5-13. Change in  $E(f)$  with diode imbalance.

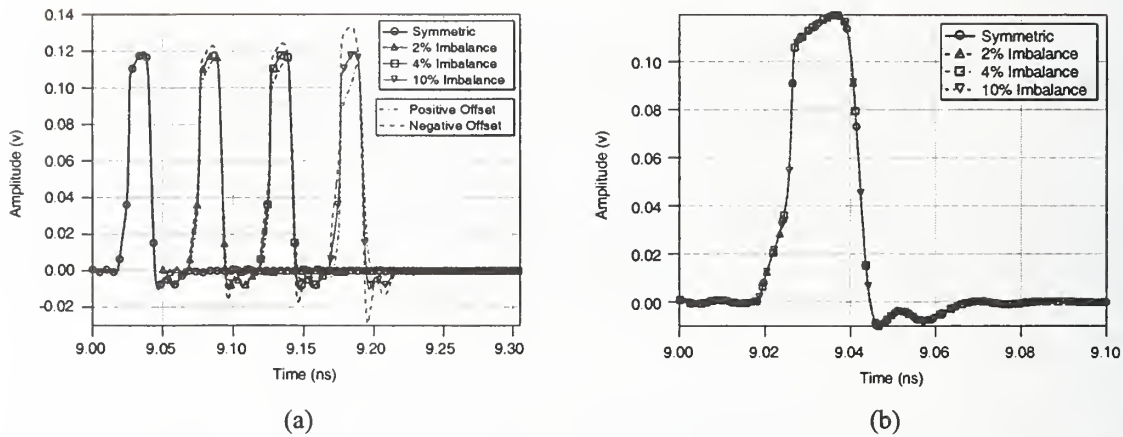


Figure 5-14. Kickout pulses with diode imbalance. (a) Dashed lines show the kickout pulses arising from negative and positive offset voltages (the inverse value of the negative-going kickout pulses has been taken). Solid lines show the average of these calculated according to eq (5-3). The time axis is shifted for better resolution of imbalanced diode cases. (b) Averaged kickout pulses (the solid lines from Fig. 5-14(a)) with no time-axis shift. The averaged kickout pulses are similar to the symmetric case.

## 5.5 Diode Bias Level

### 5.5.1 Description

The level of reverse bias on the sampling diodes will determine both how strongly the diodes conduct and their conduction time, when the strobe pulse forward-biases them into conduction. This is how we change the bandwidth of the oscilloscope. Intuitively, one may not expect these parameters to change the phase error of the nose-to-nose calibration. However, this parametric study indicates otherwise. As we saw in Sections 5.3.3 and 5.3.4, when the delay time in the undershoot of the kickout pulse increases, so does the phase error. We see this effect again here as we explore variation of the bias level around its nominal value.

The value of the bias supplies is specified as 1.63 V in our default sampler model. We varied the default value by  $\pm 20\%$  in this parametric study. We chose a limit of  $20\%$  based on simulations of the Kerley sampler model presented in Section 4.2. There we showed that the change in bias that best matched high- and low- bandwidth mode measurements was  $20\%$ . We estimate that the variation in bias level from sampler to sampler in high-bandwidth mode will be less than this.

## 5.5.2 Simulation Results

Figure 5-15 shows that the phase component of the correction factor,  $E(f)$ , increases as the reverse bias on the sampling diodes decreases, corresponding to stronger conduction and a longer conduction time for the diodes.

Figure 5-16 shows time-domain plots of the strobe pulse and the kickout pulse for three of the bias levels given in Fig. 5-15. We can again recognize the increase in error in the time domain by observing a delay in the undershoot at the falling edge of the kickout pulse. The appendix explains why the phase error increases with time delay of an error pulse such as the undershoot of the kickout pulse.

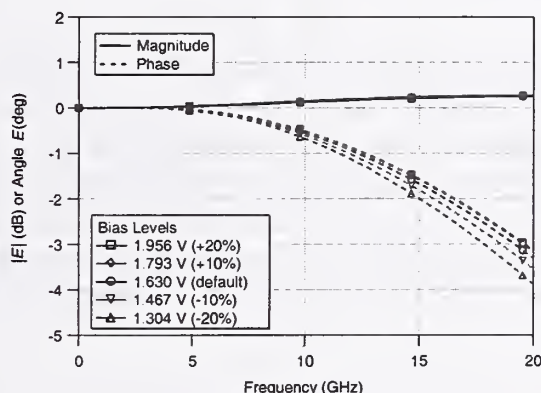


Figure 5-15.  $E(f)$  for several bias levels up to  $\pm 20\%$  of the default model value.

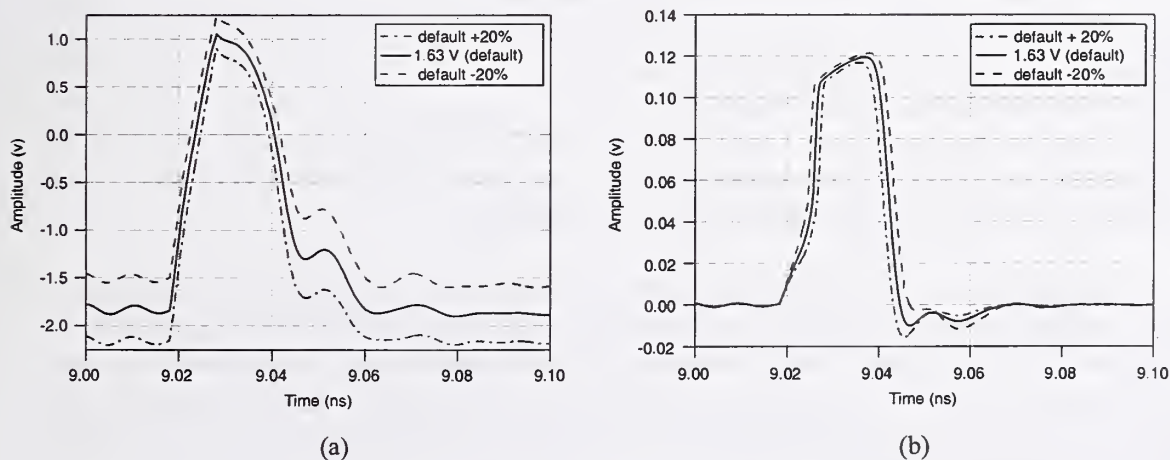


Figure 5-16. (a) Strobe pulses and; (b) Kickout pulses corresponding to three different bias levels.

## 5.6 Input Network Impedance

### 5.6.1 Description

We use mismatch correction to correct for the effects of cables and connectors joining the two oscilloscopes together in nose-to-nose calibration measurements. In our simulations, the first sampler (the kickout generator) drives an ideal  $50\ \Omega$  load and the second sampler is driven by an ideal  $50\ \Omega$  source. This ideal isolation network between the two sampling circuits simulates an infinite delay and eliminates the need for any mismatch correction.

However, between the input port of the oscilloscope and the input to the sampler lies an unknown network of filters. The errors introduced by the input filter network discussed in this section are different from the effects that require mismatch correction discussed above. Here we examine potential effects of this unknown network on the sampler response of the nose-to-nose calibration. We introduce additional impedances on the input port of each sampler, and consider the response of the network-plus-sampler combination.

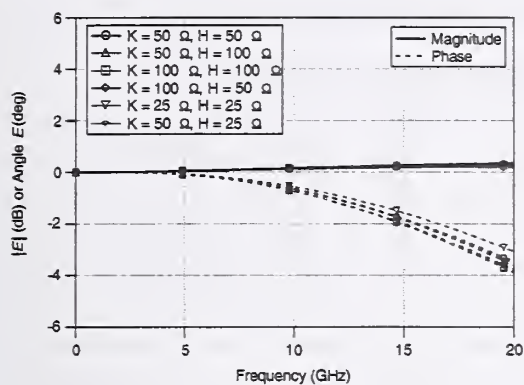
The nominal impedance at the input port of the sampling circuits used in oscilloscopes is given as  $50\ \Omega$  by both Riad [19] and Kerley [2], [24]. It is assumed to be purely resistive. Here we implement both purely resistive ( $25\ \Omega$  to  $100\ \Omega$ ) and mixed resistive/reactive input networks. The reactances are implemented as either a capacitor in parallel with the input port or an inductor in series with the input port. We chose reactances ranging in value from on the order of the diode junction capacitance ( $C = 100\ \text{pF}$  and  $L = 0.1\ \text{nH}$ ) to reactances on the order of the hold capacitors ( $C = 1\ \text{pF}$  and  $L = 1\ \text{nH}$ ).

### 5.6.2 Simulation Results

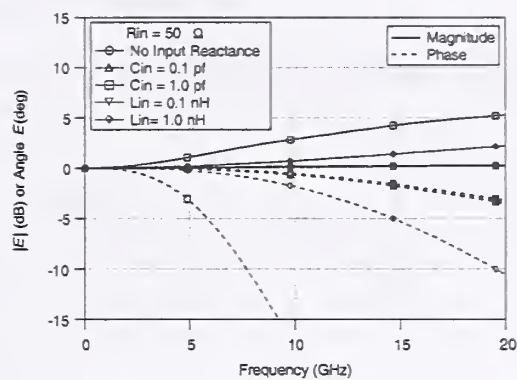
As shown in Fig. 5-17(a), if the input network is purely resistive, the correction factor  $E(f)$  is not adversely affected. However, reactances that approach the value of the hold capacitor placed at the input to the sampler may affect the correction factor of the nose-to-nose calibration, as shown in Fig. 5-17(b). This latter case may be explained by the fact that the input network begins to store charge in a manner similar to that of the hold capacitors, but the balanced strobe signal is not cancelled at the output amplifier as it is with the two-branch configuration of the hold capacitors.

Based on the simulations in this section, purely resistive input networks appear to have a negligible effect, and only reactances that approach that of the hold capacitor have an impact on the phase error in the nose-to-nose calibration. We assume that the oscilloscopes we use are manufactured to avoid the problem of highly reactive filter components; therefore, this unknown filter network is not included in the sensitivity analysis in the next section.





(a)

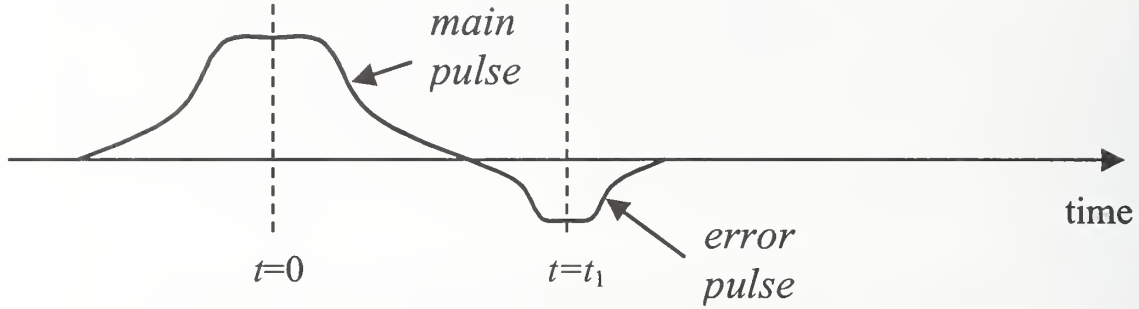


(b)

Figure 5-17.  $E(f)$  for (a) resistive input networks; (b) reactive input networks.

## Appendix for Section 5. Error Pulses

Consider a main pulse followed by a small error pulse in the time domain:



The Fourier transform pair corresponding to these pulses may be given by

$$x(t) - \alpha x(t - t_1) \leftrightarrow X(j\omega) - \alpha X(j\omega)e^{-j\omega t_1}. \quad A(1)$$

For small  $\alpha$  and small values of  $\omega t_1$ , we can use a Taylor series expansion of the form

$$e^{\pm x} = 1 \pm x + \frac{x^2}{2!} \pm \frac{x^3}{3!} + \dots \quad A(2)$$

With  $F$  equal to the right hand side of A(1)

$$\begin{aligned} F &= X(j\omega)(1 - \alpha e^{-j\omega t_1}) \\ &\cong X(j\omega)[1 - \alpha(1 - j\omega t_1 + \frac{(j\omega t_1)^2}{2} - \frac{(j\omega t_1)^3}{6} + \dots)] \\ &\cong X(j\omega)[(1 - \alpha - \alpha \frac{(\omega t_1)^2}{2}) - j\alpha(\omega t_1 + \frac{(\omega t_1)^3}{6})]. \end{aligned} \quad A(3)$$

$$\text{In this case we end up with a magnitude error of } 1 - \alpha - \alpha \frac{(\omega t_1)^2}{2}, \quad A(4)$$

$$\text{and a phase error of } \alpha\omega t_1 + \alpha \frac{(\omega t_1)^3}{6}. \quad A(5)$$

The first term of eq A(5) corresponds to a linear phase error, which we detrend from the phase component of the error ratio using the method described in Section 2.4. The second term in eq A(5) corresponds to a phase error term, whose magnitude grows as the *cube* of the time delay of the error pulse relative to the main pulse. Thus, even small error pulses can contribute significantly to the phase error when delayed relative to the main pulse. For main and error pulses that do not have the same shape, that is, for pulses not of the form  $X(j\omega) - \alpha X(j\omega)$ , we would expect to see a second-order phase-error term as well. Because our system is not linear, time-invariant, or passive, the phase function is not required to be an odd function.

## 6. Sensitivity Analysis and Standard Uncertainty

In the previous section, we demonstrated that the phase error in the nose-to-nose calibration is sensitive to variation in sampling-circuit parameter values. We will now quantify this phase-error sensitivity in two different ways. In Section 6.1, we rank the circuit parameters discussed in Section 5 with respect to impact on the phase error in the default sampling circuit. We vary each parameter by the same amount (10 %), and note the corresponding change in the phase error. The parameters causing a larger change in phase error are ranked higher. Using this procedure, we see the relative effect that variation (or uncertainty) in the value of each circuit parameter has on the phase error of the calibration. This information can be used in a variety of ways: for example, in determining which circuit elements should be modeled most carefully in sampling-circuit simulations, and which circuit elements should be considered in sampling-circuit designs for improved nose-to-nose calibrations.

In Section 6.2, we calculate the standard uncertainty in the phase error due to combined component value variation. The standard uncertainty provides us with an important piece of information: it represents our best estimate of a *range* of phase-error values due to the sampling circuitry for a real nose-to-nose calibration. Throughout this report our goal has been to accurately model the real samplers found in the type of oscilloscope used in nose-to-nose calibrations. However, uncertainty exists both in the values of some circuit parameters and in the way some circuit elements are modeled. By assuming a significant level of uncertainty for each individual circuit parameter, we hope to cover the expected range of phase errors due to the sampling-circuit mechanism in a real nose-to-nose calibration. Finally, in Section 6.3, we summarize, draw conclusions, and provide notes for future work.

### 6.1 Ranking the Contributions to the Phase-Error Uncertainty

In this section, we calculate the uncertainty (or variation) in the phase error arising from uncertainty (or variation) in the value of each circuit parameter discussed in the previous section. We do this by finding the change in the default phase-error value for a given variation in circuit parameter value. The parameters leading to greater phase error changes are ranked higher.

We define the uncertainty in the phase error due to parametric variation as the standard deviation in the phase error with respect to variation or uncertainty in a given parameter. According to Refs. [26], [27], and [28], we should calculate the standard deviation for each quantity that contributes to uncertainty using Type A evaluation and/or Type B evaluation. Type A evaluation corresponds to determination of uncertainty using statistical means based on repeated observation. Type A evaluation of uncertainty is most often used when repeated measurements, made under identical conditions, are available. Type B evaluation of uncertainty corresponds to uncertainty that is not measured statistically. We use Type B evaluation in the present work, since we are basing our calculations on individual simulations of our sampling-circuit model.

We express the uncertainty in the phase error corresponding to each parameter in our default sampling-circuit model as [26]

$$u_{\phi}(\alpha_j) = \frac{\partial \phi}{\partial \alpha_j} u_{\alpha_j}, \quad (6-1)$$

where

$\alpha_j$  = circuit parameter corresponding to parameter number  $j$ ,

$u_{\alpha_j}$  = fractional uncertainty (variation) in  $\alpha_j$  (10 % of the values given in Table 4-1),

$\phi$  = phase error in the nose-to-nose calibration simulations (with a default value of  $\sim 3.3^\circ$  at 20 GHz),

$\frac{\partial \phi}{\partial \alpha_j}$  = change in the phase error due to variation in circuit parameter value  $\alpha_j$ , and

$u_{\phi}(\alpha_j)$  = uncertainty in the phase error corresponding to the uncertainty  $u_{\alpha_j}$ .

To calculate the uncertainties expressed in eq (6-1), we performed simulations of our default model where we chose a value for the fractional uncertainty  $u_{\alpha_j}$  for each model parameter  $\alpha_j$  studied in Section 5. For comparison purposes, we chose the fractional uncertainty in each of the model parameters as the same value,  $\pm 10\%$  of  $\alpha_j$ . We selected a value of 10 % based on manufacturer's data sheets for sampling diodes that are similar to those we expect to find in the type of oscilloscopes used in nose-to-nose calibrations [25]. In these data sheets, the maximum variation in junction capacitance is approximately 10 %, so we chose this as an upper limit for our study.

For each parameter, we calculated a minimum of three sets of phase errors: the default case, one (or more) case(s) with  $\alpha_j$  increased, and one (or more) case(s) with  $\alpha_j$  decreased. We fitted a straight line to these phase errors at 20 GHz (the highest frequency considered in our default model) and numerically calculated the derivative  $[\partial \phi / \partial \alpha_j]$  of this line. We fitted the change in phase error with a straight line since our typical change in error was expected to be small (Note that for some parameters this small-value approximation does not hold, and some additional error is introduced into the uncertainty calculation.). We then multiplied the derivative (a constant value) by the fractional uncertainty  $u_{\alpha_j}$  and found the uncertainty in the phase error  $u_{\phi}(\alpha_j)$  due to this particular parameter.

Table 6-1 indicates that the strobe generator impedance (Section 5.3.3) has the most significant effect on the phase error for a fractional uncertainty of 10 % of  $\alpha_j$ , followed closely by nonlinear diode junction capacitance (Section 5.1). Previously, we mentioned that because the strobe pulse and input pulses utilize separate ground schemes in the physical sampler, the effect of the strobe generator impedance on the small-signal behavior of the sampler is difficult to accurately model. The high ranking of the strobe generator impedance simply indicates that the strobe generator model must be considered carefully when predicting the phase error of the nose-to-nose calibration.



Table 6-1. Uncertainty in the phase error in the nose-to-nose calibration at 20 GHz for the listed sampling-circuit parameter values, using the methodology discussed in Section 6.1. Contributions are ranked highest to lowest.

Parameter $\alpha_j$	Value of $\alpha_j$	$u_{\alpha_j} = 0.1\alpha_j$	$\frac{\partial\phi}{\partial\alpha_j}$	$u_\phi(\alpha_j)$
Strobe generator impedance	28.5 $\Omega$ / branch	2.9 $\Omega$	0.12°/ $\Omega$	0.35°
$C_{j0}$	0.045 pF	0.0045 pF	-70.0°/pF	0.32°
$\gamma$	0.5	0.05	-5.20°/unit	0.26°
Strobe-pulse rise time	10 ps	1 ps	-0.23°/ps	0.23°
Strobe amplitude	12 V	1.2 V	-0.16°/V	0.20°
Bias value	1.63 V	0.163 V	+1.15°/V	0.19°
$N$	1.08	0.108	-1.67°/unit	0.18°
$C_H$	4 pF	0.4 pF	-0.36°/pF	0.14°
$\phi_{bi}$	0.7 V	0.07 V	+0.82°/V	0.06°
Embedding impedance	50 $\Omega$	5 $\Omega$	-0.011°/ $\Omega$	0.05°
$I_{sat}$	20 pA	2 pA	+2.97e9°/A	0.01°
$R_s$	10 $\Omega$	---	---	not significant source of error
$E_g$	0.69 eV	---	---	not significant source of error

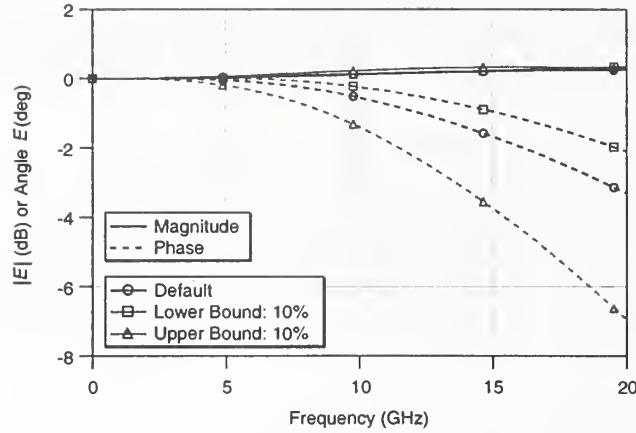


Figure 6-1. Simulations of upper and lower phase-error bounds with all parameters changed by 10%.

## 6.2 Estimate of Standard Uncertainty Due to Combined Sampling Circuitry Variation

In this section, we generate a statement of standard uncertainty using the method described in Section 4.3.8 of both Refs. [26] and [28], and Section 4.6 of Ref. [27]. This method is a Type B evaluation based on predicting the upper and lower bounds of uncertainty of a quantity of interest by varying all parameters on which it depends to the “fullest extent possible” [27]. Assuming that the quantity of interest will take a value within the upper and lower bounds with equal probability, we find the standard deviation of the corresponding rectangular distribution and use this value as the standard uncertainty.

To implement this procedure, we first estimated an upper and lower bound on the phase error in the default sampler model. We performed simulations that incorporated combined parametric variation, that is, we varied all of the circuit parameters simultaneously in such a way as to increase the phase error, and then varied all of the circuit parameters to decrease the phase error. As shown in Table 6-1, increasing some parameters increases the phase error (a positive value for  $[\partial\phi/\partial\alpha_j]$ ), while increasing some parameters decreases the phase error (a negative value for  $[\partial\phi/\partial\alpha_j]$ ).

Figure 6-1 shows the results of our combined parametric simulations with all circuit parameters  $\alpha_j$  changed simultaneously by 10 % in such a way as to increase or decrease the phase error. We see the typical default sampler phase-error value of  $3.32^\circ$  at 20 GHz. We see an increase of  $3.64^\circ$  (to  $6.96^\circ$ ) for the upper bound, and a decrease of  $1.21^\circ$  (to  $2.11^\circ$ ) for the lower bound. Note that the change in the phase error is not symmetric about the default value. References [26] and [28] address such a case in Section 4.3.8, and suggest using a standard uncertainty of

$$u_\phi = \frac{a}{\sqrt{3}}, \quad (6-2)$$

where  $2a$  is the difference between the lower bound and the upper bound, and  $a$  is given by

$$a = \frac{b_- + b_+}{2}, \quad (6-3)$$

with  $b_+$  the positive offset, and  $b_-$  the negative offset. Note that eq (6-2) corresponds to the standard deviation of a rectangular distribution from the lower bound to the upper bound, and eq (6-3) effectively shifts the mean to the middle of this distribution. The standard uncertainty  $u_\phi(\alpha)$  is then given by

$$\begin{aligned} u_\phi(\alpha) &= \sqrt{\frac{(b_+ + b_-)^2}{12}} \\ &= \sqrt{\frac{(3.64^\circ + 1.21^\circ)^2}{12}} \\ &= 1.4^\circ, \end{aligned} \quad (6-4)$$

where  $\alpha$  represents the combined set of circuit parameters. Our estimate of the phase error for our default sampling-circuit model is then  $3.32^\circ \pm 1.4^\circ$  at 20 GHz, where  $1.4^\circ$  is the numerical value of standard uncertainty  $u_\phi(\alpha)$ , and not a confidence interval.

This method of finding uncertainty was used in place of a calculation of the combined uncertainty, that would be found by appropriately combining the fractional uncertainties  $u_{\alpha_j}$  calculated in the previous subsection. To generate such a combined uncertainty statement using the method described in Section 5 of Ref. [26], we would need to know the correlation between the individual contributions to the overall uncertainty. For example, we would need to know whether a change in the grading coefficient of the sampling diode would affect the value of the diode's junction capacitance, or whether an increase in the strobe pulse rise time would lead to an increase in the strobe amplitude. We do not have this information explicitly, since much of it depends on the fabrication and design of the sampling circuit. However, we do expect some correlation to exist between certain circuit parameters, and so cannot ignore potential correlation effects.

If we were to assume no correlation between the circuit parameters, the uncertainties  $u_{\phi_j}(\alpha_j)$  listed in Table 6-1 would add in a root-sum-of-squares (RSS) sense to give the combined uncertainty. If we were to assume complete correlation, the uncertainties listed in Table 6-1 would add directly. We expect that the combined uncertainty for the phase error in the sampling circuit lies somewhere between these two. Note that if we combined the uncertainties calculated in Section 6.1 linearly (complete correlation),  $u_\phi(\alpha)$  would be  $2.96^\circ$ , and if we combined the uncertainties in the RSS sense,  $u_\phi(\alpha)$  would be  $0.98^\circ$ . Our estimate lies between these two extremes.

We expect that the phase error in our default model of  $3.32^\circ \pm 1.4^\circ$  at 20 GHz is higher than that of real sampling circuits simply because our model is based on conservative approximations and assumptions. For example, our model of the sampling diode uses a single term for the zero-bias junction capacitance  $C_{j0}$ . In Section 5.1, a Split Diode Model was discussed where the total capacitance was distributed between a lower  $C_{j0}$  value and a linear, parasitic packaging capacitance. We mentioned that this model is probably a more accurate diode model than the one used in our default sampler. The phase error in that model is around  $2^\circ$ , lower than our default sampler phase error. Thus, while our default model provides an estimate of sampler behavior, we know it may be enhanced by further study.

### 6.3 Summary and Conclusions

We performed a sensitivity study of the effect of sampling-circuit parameter-value variation on the phase error in the nose-to-nose calibration. We first defined a way to express the difference between our nose-to-nose-derived estimate of the impulse response of the sampler and the actual impulse response. We then developed a SPICE model of the sampling circuit as a mechanism to explore the effects of parametric variation. We performed simulations of two sampling circuits connected nose-to-nose, calculated an estimate of the sampler's response, and determined the phase error in our estimate. We then observed the change in the phase error as we individually varied each circuit parameter. We ranked the circuit parameters in terms of most significant impact on the phase error for a given parametric variation (10 % of the default value), and found the standard uncertainty of the phase error with respect to this parametric variation.

For our default sampling-circuit model, we calculated a phase error of  $3.32^\circ \pm 1.4^\circ$ . By assuming a significant level of uncertainty for each individual circuit parameter, our intent has been to cover the expected range of phase errors in a real nose-to-nose calibration. This provides us with a first-cut estimate of the contribution of the sampling circuitry to the phase error in the nose-to-nose calibration, since, as mentioned in Section 1.1, this quantity cannot be measured directly.

Our parametric studies indicate that both the diode nonlinear junction capacitance and the strobe generator impedance have a significant influence on the total phase error. Thus, while overall refinement of the sampling-circuit model will provide a more accurate estimate of the phase error, we expect that refining the diode model and the strobe generator model in particular will help to more accurately determine both the expected phase error due to the sampling circuitry and the uncertainty in that phase error.

---

The author is grateful to the following people for help with models, theory, and discussion of the nose-to-nose calibration: Dylan Williams, Don DeGroot, Jan Verspecht, Marc Vanden Bossche, Frans Verbeyst, John Kerley, Paul Hale, Tracy Clement, Jim Randa.



## References

- [1] Rush, K.; Draving, S; and Kerley, J. Characterizing high-speed oscilloscopes. *IEEE Spectrum*: 38-39; Sept. 1990.
- [2] Verspecht, J.; Rush, K. Individual characterization of broadband sampling oscilloscopes with a nose-to-nose calibration procedure. *IEEE Trans. Instrum. Meas.* 43: 347-354; Apr. 1994.
- [3] Verspecht, J. Broadband sampling oscilloscope characterization with the 'nose-to-nose' calibration procedure: A theoretical and practical analysis. *IEEE Trans. Instrum. Meas.* 44: 991-997; Dec. 1995.
- [4] Verspecht, J. Calibration of a Measurement System for High Frequency Nonlinear Devices. Brussels, Belgium: Vrije Univeriteit Brussels, Ph.D. Thesis; Sept. 1995.
- [5] Hale, P.D.; Clement, T.S.; Coakley, K.J.; Wang, C.M.; DeGroot, D.C.; Verdoni, A.P. Estimating the magnitude and phase response of a 50 GHz sampling oscilloscope using the 'Nose-to-Nose' method. *55th ARFTG Conf. Dig.*: 35-42; June 2000.
- [6] Gans, W.L. Dynamic calibration of waveform recorders and oscilloscopes using pulse standards. *IEEE Trans. Instrum. Meas.* 39: 952-957; Dec. 1990.
- [7] Deyst, J.P.; Paulter, N.G.; Daboczi, T.; Stenbakken, G.N.; Souders, T.M. A fast-pulse oscilloscope calibration system. *IEEE Trans. Instrum. Meas.* 47: 1037-1041; Oct. 1998.
- [8] Kolner, B.H.; Bloom, D.M. Electrooptic sampling in GaAs integrated circuits. *IEEE J. Quantum Electron.* QE-22: 79-93; Jan. 1986.
- [9] Williams, D.F.; Hale, P.D.; Clement, T.S.; Morgan, J.M. Calibrating electro-optic sampling systems. *IEEE MTT-S Int. Microwave Symp. Dig.*: 1527-1530; May 2001.
- [10] Henderson, D.; Roddie, A.G.; Smith, A.J.A. Recent developments in the calibration of fast sampling oscilloscopes. *IEE Proc. A* 139: 254-260; Sept. 1992.
- [11] Lott, U. Measurement of magnitude and phase of harmonics generated in nonlinear microwave two-ports. *IEEE Trans. Microwave Theory Tech.* 37: 1506-1511; 1989.
- [12] DeGroot, D.C.; Hale, P.D.; Vanden Bossche, M.; Verbeyst, F.; and Verspecht, J. Analysis of interconnection networks and mismatch in the nose-to-nose calibration. *55th ARFTG Conf. Dig.*: 116-121; June 2000.
- [13] Larson, D.R.; Paulter, N.G. The effects of offset voltage on the amplitude and bandwidth of kick-out pulses used in the nose-to-nose sampler impulse response characterization method. *IEEE Trans. Instrum. Meas.* 50: 872-876; Aug. 2001.
- [14] Verspecht, J. Quantifying the maximum phase-distortion error introduced by signal samplers. *IEEE Trans. Instrum. Meas.* 46: 660-666; June 1997.
- [15] Williams, D.F.; Remley, K.A. Analytic sampling-circuit model. *IEEE Trans. Microwave Theory Tech.* 49: 1013-1019; June 2001.
- [16] Williams, D.F.; Remley, K.A.; DeGroot, D.C. Nose-to-nose response of a 20-GHz sampling circuit. *54th ARFTG Conf. Dig.*: 64-70; Dec. 1999.
- [17] Remley, K.A.; Williams, D.F.; DeGroot, D.C. Realistic sampling-circuit model for a nose-to-nose calibration. *IEEE MTT-S Int. Microwave Symp. Dig.*: 1473-1476; June 2000.

- [18] Bailey, A.E. Microwave Measurements, 2nd ed. London: Institute of Electrical Engineers: Ch. 16 "Sampling Systems," by P. Cochrane: 360-384; 1972.
- [19] Riad S. Modeling of the HP-1430A feedthrough wideband (28-ps) sampling head. IEEE Trans. Instrum. Meas. IM-31: 110-115; June 1982.
- [20] Remley, K.A.; Williams, D.F.; DeGroot, D.C.; Verspecht, J.; Kerley, J. Effects of nonlinear diode junction capacitance on the nose-to-nose calibration. IEEE Microwave and Wireless Comp. Lett. 11: 196-198; May 2001.
- [21] Maas, S.A. Microwave Mixers, 2nd ed. Boston, MA: Artech House; 1993.
- [22] Vladimirescu, A. The SPICE Book. New York: Wiley and Sons; 1994.
- [23] Neudeck, G.W. The PN Junction Diode, 2nd ed. Reading, MA: Addison-Wesley; 1989.
- [24] Kerley, J., Agilent Technologies, Colorado Springs, CO, Direct Communication; March 1991.
- [25] Agilent Technologies Inc. Data Sheet: HSCH-9101/9201/9251 GaAs Beam Lead Schottky Barrier Diodes; 2001.
- [26] American National Standards Institute. U.S. Guide to the Expression of Uncertainty in Measurement; Boulder, CO: National Conference of Standards Laboratories; 1997.
- [27] Taylor, B.N.; Kuyatt, C.E. Guidelines for evaluating and expressing the uncertainty of NIST measurement results. National Institute of Standards and Technology; NIST Tech. Note 1297; 1994.
- [28] International Organization for Standardization (ISO). Guide to the Expression of Uncertainty in Measurement. Geneva, Switzerland; 1995.

# *NIST* Technical Publications

## *Periodical*

---

**Journal of Research of the National Institute of Standards and Technology**—Reports NIST research and development in metrology and related fields of physical science, engineering, applied mathematics, statistics, biotechnology, and information technology. Papers cover a broad range of subjects, with major emphasis on measurement methodology and the basic technology underlying standardization. Also included from time to time are survey articles on topics closely related to the Institute's technical and scientific programs. Issued six times a year.

## *Nonperiodicals*

---

**Monographs**—Major contributions to the technical literature on various subjects related to the Institute's scientific and technical activities.

**Handbooks**—Recommended codes of engineering and industrial practice (including safety codes) developed in cooperation with interested industries, professional organizations, and regulatory bodies.

**Special Publications**—Include proceedings of conferences sponsored by NIST, NIST annual reports, and other special publications appropriate to this grouping such as wall charts, pocket cards, and bibliographies.

**National Standard Reference Data Series**—Provides quantitative data on the physical and chemical properties of materials, compiled from the world's literature and critically evaluated. Developed under a worldwide program coordinated by NIST under the authority of the National Standard Data Act (Public Law 90-396). NOTE: The Journal of Physical and Chemical Reference Data (JPCRD) is published bimonthly for NIST by the American Institute of Physics (AIP). Subscription orders and renewals are available from AIP, P.O. Box 503284, St. Louis, MO 63150-3284.

**Building Science Series**—Disseminates technical information developed at the Institute on building materials, components, systems, and whole structures. The series presents research results, test methods, and performance criteria related to the structural and environmental functions and the durability and safety characteristics of building elements and systems.

**Technical Notes**—Studies or reports which are complete in themselves but restrictive in their treatment of a subject. Analogous to monographs but not so comprehensive in scope or definitive in treatment of the subject area. Often serve as a vehicle for final reports of work performed at NIST under the sponsorship of other government agencies.

**Voluntary Product Standards**—Developed under procedures published by the Department of Commerce in Part 10, Title 15, of the Code of Federal Regulations. The standards establish nationally recognized requirements for products, and provide all concerned interests with a basis for common understanding of the characteristics of the products. NIST administers this program in support of the efforts of private-sector standardizing organizations.

*Order the following NIST publications—FIPS and NISTIRs—from the National Technical Information Service, Springfield, VA 22161.*

**Federal Information Processing Standards Publications (FIPS PUB)**—Publications in this series collectively constitute the Federal Information Processing Standards Register. The Register serves as the official source of information in the Federal Government regarding standards issued by NIST pursuant to the Federal Property and Administrative Services Act of 1949 as amended, Public Law 89-306 (79 Stat. 1127), and as implemented by Executive Order 11717 (38 FR 12315, dated May 11, 1973) and Part 6 of Title 15 CFR (Code of Federal Regulations).

**NIST Interagency or Internal Reports (NISTIR)**—The series includes interim or final reports on work performed by NIST for outside sponsors (both government and nongovernment). In general, initial distribution is handled by the sponsor; public distribution is handled by sales through the National Technical Information Service, Springfield, VA 22161, in hard copy, electronic media, or microfiche form. NISTIR's may also report results of NIST projects of transitory or limited interest, including those that will be published subsequently in more comprehensive form.

**National Institute of Standards and Technology**

Technology Administration

U.S. Department of Commerce

325 Broadway

Boulder, CO 80305-3328

**Official Business**

Penalty for Private Use, \$300